AIMS Mathematics, 11(6): 17239–17292.
DOI: 10.3934/math.2026707
Received: 26 March 2026
Revised: 02 May 2026
Accepted: 19 May 2026
Published: 15 June 2026

http://www.aimspress.com/journal/Math

Research article

Mathematical modeling of COVID-19 and chronic kidney disease co-infection with vaccination and optimal control: a bifurcation and sensitivity analysis approach

Mallela Ankamma Rao[1], Emad K Jaradat[2], Medisetty Padma Devi[3], Prasantha Bharathi Dhandapani[4,*], Carlos Martin-Barreiro[5] and Mohannad Al-Hmoud[2]

[1] Department of Mathematics & Statistics, Vignan's Foundation for Science, Technology & Research (Deemed to be University), Yadadri Bhuvanagiri 508284, Telangana, India
[2] Department of Physics, Faculty of Science, Imam Mohammad Ibn Saud Islamic University (IMSIU), Riyadh 11623, Saudi Arabia
[3] Department of Mathematics & Statistics, Vignan's Foundation for Science, Technology & Research (Deemed to be University), Vadlamudi, Guntur 522213, Andhra Pradesh, India
[4] Department of Mathematics, Sri Eshwar College of Engineering, Coimbatore 641202, Tamil Nadu, India
[5] Facultad de Ingeniería, Universidad Espíritu Santo, Samborondón 0901952, Ecuador

* **Correspondence:** Email: d.prasanthabharathi@gmail.com.

Abstract: Chronic kidney disease (CKD), affecting approximately 843 million individuals globally, substantially increases susceptibility to severe COVID-19 outcomes, while SARS-CoV-2 infection independently accelerates renal deterioration through cytokine storms and microvascular injury. Despite this clinically significant bidirectional interaction, rigorous mathematical characterization of their co-dynamics within a unified framework integrating stability theory, bifurcation analysis, and optimal control remains limited. We formulated a seven-compartment deterministic model incorporating CKD'S irreversibility, the enhanced blue susceptibility of CKD patients, and vaccine imperfection, calibrated against Indian epidemiological data. The basic reproduction number $\mathcal{R}_0$ was derived using the next-generation matrix method, and stability and bifurcation analysis were performed. Sensitivity analysis identified transmission and immunity waning as dominant drivers, while optimal control strategies significantly reduced co-infections and hospitalizations, demonstrating the effectiveness of coordinated intervention policies.

Keywords: COVID-19; chronic kidney disease (CKD); co-infection model; basic reproduction number; stability analysis; bifurcation analysis; sensitivity analysis; optimal control theory
Mathematics Subject Classification: 92D30, 34D20, 37N25, 49J15, 93A30

1. Introduction

Coronavirus disease 2019 (COVID-19), caused by severe acute respiratory syndrome coronavirus 2 (SARS-CoV-2), emerged in late 2019 and rapidly evolved into a global pandemic responsible for over 700 million confirmed cases and more than 7 million deaths worldwide [1]. The RNA-based genome of SARS-CoV-2 undergoes frequent mutations, giving rise to variants with altered transmissibility, pathogenicity, and immune escape capacity. Variants of concern, including Alpha (B.1.1.7), Delta (B.1.617.2), and Omicron (B.1.1.529), demonstrated substantial spike protein mutations that compromised vaccines' effectiveness, elevated the reinfection risk, and modified transmission intensity [2,3]. These evolutionary pressures arise from host immune responses and large-scale vaccination campaigns, underscoring the continued necessity of genomic surveillance, adaptive vaccination strategies, and evidence-based public health responses [4].

Chronic kidney disease (CKD) is a progressive, largely irreversible non communicable disorder characterized by sustained deterioration of renal function over months to years. Globally, CKD affects an estimated 843 million individuals and accounts for approximately 1.2 million deaths annually, imposing an enormous and growing burden on health systems worldwide [5, 6]. The principal etiological drivers are diabetes mellitus and hypertension, both of which progressively damage the renal microvasculature and glomerular architecture [7]. Additional causes include glomerulonephritis, polycystic kidney disease, nephrotoxic exposures, and recurrent acute kidney injury (AKI) [8]. Although advanced CKD is not reversible, early detection and sustained clinical management can meaningfully retard its progression [9]. Contemporary therapeutic strategies encompass strict glycemic and blood pressure control, renin–angiotensin–aldosterone system (RAAS) inhibitors, sodium–glucose cotransporter-2 (SGLT2) inhibitors, mineralocorticoid receptor antagonists, and structured lifestyle interventions [10]. Crucially, unlike acute infectious diseases, CKD introduces permanent physiological vulnerability, persistent systemic inflammation, and progressive cumulative organ damage that fundamentally alters the host's responses to concurrent infections.We emphasize at the outset that CKD is non communicable: A CKD patient does not generate new CKD cases through person-to-person contact. Throughout this paper, the population-level CKD incidence is captured by a constant per-capita non communicable hazard λ_k rather than by a transmission coefficient. Furthermore, because CKD is irreversible, hospitalized CKD patients who clinically improve from hospitalization cannot "recover" into a recovered class; they instead return to the CKD patient class, a modelling subtlety that motivates the H-recovery splitting introduced in Section 2.

The coexistence of COVID-19 and CKD generates a clinically and epidemiologically significant dual burden. CKD patients exhibit immune dysregulation, chronic low-grade inflammation, and endothelial dysfunction that substantially amplify susceptibility to severe SARS-CoV-2 infection and adverse outcomes [11]. Conversely, SARS-CoV-2 directly impairs renal function through viral tropism for tubular epithelial cells, cytokine storms,, microvascular thrombosis, and hemodynamic instability, accelerating CKD's progression or precipitating AKI superimposed on pre-existing renal impairment [12]. Recent compartmental models, including the six-compartment framework of Ambalarajan et al. [13], have advanced the mathematical analysis of COVID-19 transmission and intervention design; however, such models do not incorporate chronic comorbidities such as CKD, leaving the dual-burden dynamics of infectious and irreversible noncommunicable diseases analytically unaddressed.

Cohort evidence demonstrates that COVID-19 is independently associated with accelerated long-term renal decline compared with other respiratory infections [14], and CKD patients infected with COVID-19 experience markedly higher rates of hospitalization, dialysis initiation, and mortality [12]. Notably, large-scale analyses indicate that even individuals without AKI at the time of infection face a substantially elevated risk of developing advanced CKD during follow-up [15]. Furthermore, the immune suppression intrinsic to CKD is known to attenuate vaccine-induced immunity, reducing the effective protection conferred by COVID-19 vaccines in this population and providing direct biological motivation for the vaccine imperfection parameter incorporated in the present model [11, 12]. These converging lines of evidence underscore the urgent need for integrated analytical frameworks that simultaneously address infectious transmission dynamics and irreversible chronic disease progression [16].

Mathematical modeling plays a central and expanding role in quantifying infectious disease transmission, identifying epidemiological thresholds, and evaluating competing intervention strategies. Deterministic compartmental models translate biological mechanisms into tractable dynamical systems that permit the derivation of threshold quantities such as the basic reproduction number $\mathcal{R}_0$ and the time-varying reproduction number $\mathcal{R}_t$, an analytical characterization of equilibrium stability, and a systematic comparison of public health policies [17, 18]. Recent methodological advances include hybrid mechanistic–machine learning frameworks that enhance spatial forecasting accuracy [19], nonlinear incidence formulations with behavioral feedback [20], region-specific models incorporating demographic heterogeneity [21], and rigorous uncertainty quantification approaches combining Latin hypercube sampling with partial rank correlation coefficient (PRCC) analysis [22]. These developments collectively emphasize the importance of integrating analytical rigor, parameter identifiability, and sensitivity assessment to produce reliable, policy-relevant quantitative insights.

A growing body of mathematical literature has examined COVID-19-related co-infection dynamics with both infectious and chronic conditions. Deterministic models of COVID-19 and typhoid fever have characterized joint transmission dynamics and derived optimal treatment strategies via Pontryagin's maximum principle [23]. COVID-19–tuberculosis co-infection models have revealed threshold behavior, backward bifurcation phenomena, and the potential for disease persistence even when $\mathcal{R}_0 < 1$ [24, 25]. Investigations of COVID-19 pneumonia and COVID-associated pulmonary aspergillosis (CAPA) have demonstrated synergistic reductions under combined vaccination and treatment interventions [26]. Models coupling COVID-19 with noncommunicable diseases such as diabetes and hypertension have highlighted how chronic comorbidities modify the transmission thresholds and equilibrium infection levels [21]. Of particular relevance, Hye et al. [27] proposed a compartmental model for COVID-19 and kidney disease co-infection; however, that study did not fully incorporate vaccination dynamics as a structural compartment, did not perform a bifurcation analysis to characterize the threshold behavior at $\mathcal{R}_0 = 1$, and did not formulate a time-dependent optimal control problem, leaving the quantitative assessment of coordinated intervention strategies and long-term persistence mechanisms arising from the infectious–chronic disease coupling structure unaddressed.

Despite these contributions, a rigorous mathematical analysis of COVID-19 interacting with a chronic, irreversible noncommunicable disease such as CKD within a single framework that simultaneously integrates compartmental modeling, local stability and bifurcation analysis, global sensitivity assessment, and multi-control optimal control theory remains, to our knowledge, absent

from the literature. Four structural gaps are particularly significant. First, the irreversible nature of CKD—whereby individuals cannot recover from the CKD compartment—introduces qualitatively distinct persistence mechanisms that differ fundamentally from acute–acute co-infection models and have not been analytically characterized from a threshold and bifurcation perspective. Second, the enhanced susceptibility of CKD patients to COVID-19 and the consequent amplification of co-infection burden requires explicit structural representation, rather than a simple additive comorbidity assumption, to correctly capture transmission threshold behavior. Third, the joint optimization of vaccination, clinical management and hospital triage, and recovery from hospitalization as coordinated time-dependent controls has not been formulated or solved for this disease pairing, leaving a critical gap in quantitative intervention guidance. Fourth, the heterogeneous composition of the hospitalized class H—which simultaneously contains COVID-active and CKD-only patients—and the consequent biological requirement that hospitalized CKD patients return to the CKD class (rather than to "recovery") upon clinical improvement has not been treated rigorously in previous co-infection models; the present work introduces a dimensionless splitting fraction p that resolves this issue without violating mass conservation.

Motivated by these gaps, the present study develops and rigorously analyzes a deterministic seven-compartment model describing the co-dynamics of COVID-19 and CKD. The model partitions the total population into the susceptible (S), vaccinated (V), COVID-19 infected (I_c), CKD patients (I_k), acutely co-affected (I_{ck}), hospitalized (H), and recovered (R) compartments. Five structural features distinguish this framework from existing co-infection models. First, CKD's irreversibility is explicitly encoded: Individuals in I_k cannot transition to the recovered class, capturing the permanent nature of chronic renal impairment. Second, an immune modulation factor $0 < \alpha \leq 1$ governs the COVID-19 acquisition rate in CKD patients, reflecting the net effect of the altered immune micro environment on community-level contact-to-infection conversion as documented in non-dialysis CKD cohorts [28]. Third, vaccines' imperfection is represented through a failure parameter $(1 - \varepsilon_v)$, acknowledging the attenuated vaccine-induced immunity documented in CKD cohorts. Fourth, the bidirectional progression pathways between acute infection and chronic disease states are captured through the transition rates θ (the rate of COVID-19-induced AKI onset, capturing the rapid renal complications observed in a subset of COVID-19 patients rather than a transition to clinically established CKD.) and γ_{ck} (partial recovery from the acutely co-affected state to CKD only), enabling the model to represent the full spectrum of clinical trajectories. Fifth, the recovery flow from the hospitalized class is split using a dimensionless fraction $p \in [0, 1]$ so that COVID-hospitalized patients enter the recovered class while CKD-hospitalized patients return to the CKD patient class upon clinical improvement; this construction preserves total population conservation while respecting CKD's irreversibility. The recovered class equation is also corrected to include the immunity loss outflow explicitly, restoring exact mass balance with the susceptible class; the precise formulations are detailed in Section 2.

The analytical contributions of this study are fourfold. The basic reproduction number $\mathcal{R}_0 = \mathcal{R}_{0c}$ is derived using the next-generation matrix method [17], reflecting the fact that CKD is a non communicable chronic condition and therefore contributes no infectious secondary cases at the disease-free equilibrium; the long-run CKD prevalence is tracked separately through a dimensionless invasion index C_k introduced in Section 3.2.1. We emphasize that C_k is not a basic reproduction number—since CKD is non communicable, the next-generation matrix for the CKD pathway is identically zero in the strict epidemiological sense—but is rather a dimensionless ratio governing

the linearized CKD-prevalence threshold under the constant non communicable hazard λ_k. The local asymptotic stability of the disease-free and the COVID-19 dominant boundary equilibria is established through linearization and spectral analysis. Bifurcation behavior at the critical threshold $\mathcal{R}_0 = 1$ is examined using the Castillo-Chavez and Song center manifold framework [29], confirming a forward (supercritical) bifurcation and precluding backward bifurcation under the assumed parameter regime. The existence of a non-trivial co-endemic equilibrium in which all three infected compartments are simultaneously positive is established numerically when both $\mathcal{R}_{0c}$ and C_k exceed unity, and the qualitative coexistence picture is verified to be robust to the choice of the H-recovery splitting fraction p over a biologically plausible range; a complete analytical characterisation of this co-endemic state is identified as a direction for future work. Normalized forward sensitivity indices and PRCC-based global sensitivity analyses [22, 30] are used to identify the parameters that most strongly govern infection dynamics and to quantify robustness under parameter uncertainty. An optimal control problem is formulated incorporating three time-dependent controls—vaccination (u_1), clinical management and hospitalization control (u_2), and enhanced recovery from hospitalization (u_3)—formulated to augment (rather than replace) the baseline rates, so that the uncontrolled baseline is recovered when the controls are set to zero. The H-recovery splitting is preserved under control, generalising the projection formula for the recovery control u_3^* to a weighted shadow price of its two destinations (the recovered class and the CKD patient class). Optimality conditions are derived via Pontryagin's maximum principle [31] and solved numerically using the forward–backward sweep method with a fourth-order Runge–Kutta (RK4) scheme [32].

By coupling a chronic irreversible disease with an acute viral infection and integrating stability theory, bifurcation analysis, global sensitivity assessment, and multi-control optimal control within a single coherent analytical framework, this study advances the mathematical understanding of dual-burden epidemics. The results provide both a rigorous theoretical characterization of long-term persistence mechanisms arising from the infectious–chronic disease coupling structure, and quantitative guidance for designing coordinated, cost-effective public health strategies in populations simultaneously affected by COVID-19 and CKD.

2. Mathematical model formulation

In this study, we develop a compartmental epidemiological model to analyze the co-infection dynamics of COVID-19 and CKD. The model comprises seven compartments representing distinct health states of the human population at any given time: Susceptible individuals (S), vaccinated individuals (V), individuals infected with COVID-19 only (I_c), individuals living with CKD only (I_k),individuals acutely co-affected by COVID-19 and CKD (I_{ck}), hospitalized individuals (H), and recovered individuals (R). The total population at time t is given by

$$N(t) = S(t) + V(t) + I_c(t) + I_k(t) + I_{ck}(t) + H(t) + R(t).$$

The schematic diagram illustrating the movement between compartments is presented in Figure 1. Based on the interactions shown in the figure and the underlying epidemiological assumptions, the model is governed by the following system of nonlinear ordinary differential equations.

Throughout this paper we use CKD patients (or individuals living with CKD) rather than "CKD infected individuals," since CKD is a non communicable chronic condition and the term

"infected" is biologically inappropriate. The compartment I_{ck} represents the acutely co-affected subgroup (individuals with COVID-19 and concurrent acute renal involvement), not individuals with simultaneously established chronic CKD plus active COVID-19.

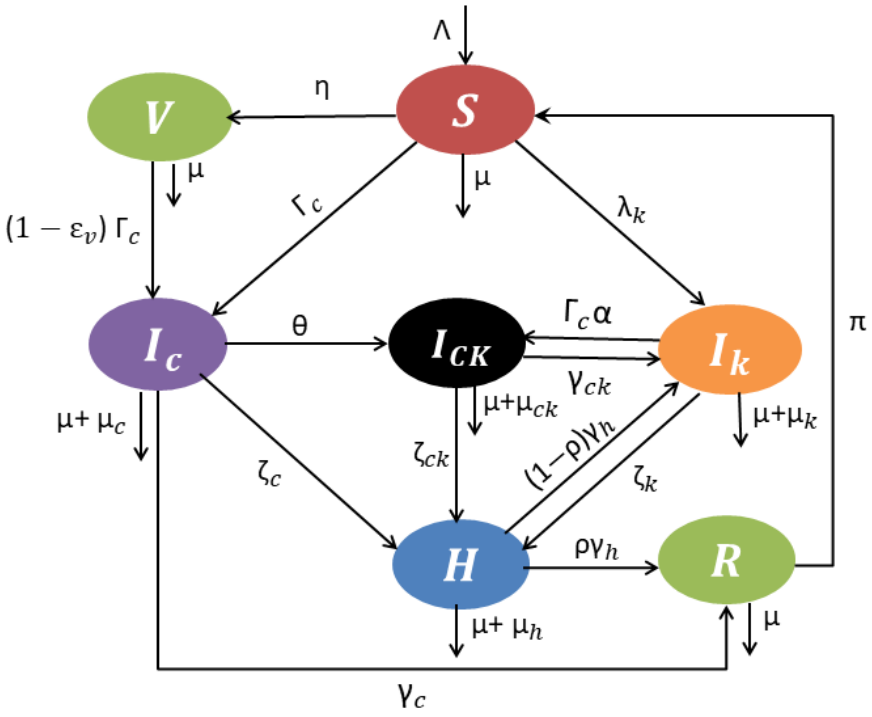

Figure 1. Schematic representation of the COVID-19 and CKD co-infection model.

Susceptible individuals (S)**.** The susceptible class consists of individuals who are at risk of acquiring COVID-19, CKD, or both. The susceptible population grows through recruitment at a constant rate Λ, representing birth and immigration, and through the return of recovered individuals who lose immunity at a rate πR. Susceptible individuals leave this class via three pathways. The first pathway is infection with COVID-19 through contact with infectious individuals (COVID-19 only, co-affected, or hospitalized) at the force of infection

$$\Gamma_c = \frac{\beta_c(I_c + I_{ck} + H)}{N},$$

where hospitalized individuals are included with weight unity for notational simplicity, but only the COVID-19-active sub population of H contributes biologically to onward transmission. In practice, hospital isolation reduces the effective infectiousness of COVID-19 H relative to community-circulating cases; this attenuation is absorbed into the calibrated value of β_c. The compartment H also contains hospitalized CKD-only patients who are not infectious for COVID-19, but because I_k enters the force of infection only through the cross-coupling term that vanishes at the disease-free state, this heterogeneity does not affect the threshold derivation. The second pathway is progression to CKD at a constant per-capita non–communicable incidence rate λ_k, representing the population-level effect of diabetes, hypertension, aging, and other non-transmission risk factors (note that $\lambda_k S$ is mathematically

and biologically distinct from the COVID-19 force of infection above and does not encode person-to-person transmission). The third pathway is transition to the vaccinated class at a rate η. Natural death occurs in all compartments at a rate μ. The dynamics of the susceptible population are governed by

$$\frac{dS}{dt} = \Lambda + \pi R - \frac{\beta_c(I_c + I_{ck} + H)}{N} S - \lambda_k S - (\eta + \mu)S.$$

Vaccinated individuals (V). This compartment captures individuals who have received a COVID-19 vaccine. Susceptible individuals enter this class at a vaccination rate η. Due to imperfect vaccine protection, vaccinated individuals remain susceptible to COVID-19 with a reduced susceptibility governed by the vaccine failure rate $(1-\epsilon_v)$, and may still acquire the infection at rate $(1-\epsilon_v)\frac{\beta_c(I_c+I_{ck}+H)}{N}$. Vaccinated individuals are not protected against CKD, which is modeled independently, and exit this class only through natural death at a rate μ. In the optimal control formulation (Section 5), the vaccination control $u_1(t)$ augments the fixed background rate η via $(\eta + \varepsilon_1 u_1)$ rather than replacing it, ensuring that $u_1 = 0$ recovers the uncontrolled baseline. The compartment dynamics are described by

$$\frac{dV}{dt} = \eta S - (1 - \epsilon_v)\frac{\beta_c(I_c + I_{ck} + H)}{N} V - \mu V.$$

COVID-19 infected individuals (I_c). The class I_c includes individuals infected with COVID-19 only, with no pre-existing CKD. Individuals enter this class from both the susceptible and vaccinated populations upon exposure to COVID-19, co-affected, or hospitalized individuals. The total inflow rate is

$$\frac{\beta_c(I_c + I_{ck} + H)}{N}(S + (1 - \epsilon_v)V),$$

which accounts for the contribution of vaccine failure. Individuals in this class may progress to the acutely co-affected class I_{ck} due to COVID-19-induced AKI at a rate θ. We emphasize that θ does not represent a transition to clinically established CKD (which, by definition, requires sustained renal impairment over > 3 months); rather, it captures the rapid onset of acute renal complications in a subset of COVID-19 patients, consistent with documented AKI rates of approximately 20%–40% in hospitalized COVID-19 cohorts and a transition timescale of days. The associated value $\theta = 0.36\ \text{day}^{-1}$ corresponds to a mean transition time of approximately 2.8 days, which is biologically plausible for the onset of AKI. redThey may also be hospitalized at a rate ζ_c, recover directly at a rate γ_c, or die from COVID-19 at a rate μ_c or from natural causes at a rate μ. The governing equation is

$$\frac{dI_c}{dt} = \frac{\beta_c(I_c + I_{ck} + H)}{N}(S + (1 - \epsilon_v)V) - (\theta + \zeta_c + \gamma_c + \mu_c + \mu)\, I_c.$$

CKD patients (I_k). This compartment contains individuals who have developed CKD independently of any COVID-19 infection. New entrants arrive from three sources: (i) The susceptible class at the constant per-capita non communicable incidence rate λ_k, reflecting background CKD incidence driven by aging, diabetes, hypertension and other non-transmission risk factors; (ii) the co-affected class I_{ck} at a rate γ_{ck}, representing partial recovery from the acute COVID-19 episode while retaining the underlying CKD; and (iii) the hospitalized class H at a rate $(1-p)\,\gamma_h$, representing the hospitalized CKD patient subgroup who clinically improve from hospitalization but, because CKD is irreversible, return

to the CKD-only class I_k rather than the recovered class R. The value $\gamma_{ck} = 0.067$ day^{-1} corresponds to a mean transition time of approximately 15 days from being co-affected back to having CKD-only, consistent with the documented clinical timeline for COVID-19's resolution in CKD patients [27]. CKD patients are at risk of acquiring COVID-19 at the modified rate $\frac{\alpha\beta_c(I_c+I_{ck}+H)}{N}$, where $0 < \alpha \leq 1$ is a susceptibility modification factor reflecting the net population-level effect of immune dysregulation in CKD patients on the contact-to-infection conversion rate. The value $\alpha = 0.46$ captures the reduced mucosal immune responsiveness at the community incidence level and is consistent with cohort-level estimates reported for non-dialysis CKD populations [28]. CKD patients may also be hospitalized at a rate ζ_k or die from CKD-related mortality μ_k or natural death μ. Since CKD is a chronic and irreversible condition, no direct recovery term to R is included for this compartment. The equation for this compartment is

$$\frac{dI_k}{dt} = \lambda_k S + \gamma_{ck} I_{ck} + (1-p)\,\gamma_h\, H - \frac{\alpha\beta_c(I_c + I_{ck} + H)}{N}\, I_k - (\zeta_k + \mu_k + \mu)\, I_k.$$

Acutely co-affected individuals (I_{ck}). The class I_{ck} includes individuals simultaneously carrying COVID-19 with concurrent acute kidney involvement (i.e., COVID-19 plus AKI, rather than COVID-19 plus established chronic CKD; see the note on θ above). This class is populated via two pathways: CKD patients who acquire COVID-19 at a rate $\frac{\alpha\beta_c(I_c+I_{ck}+H)}{N}$, and COVID-19 patients who develop acute renal complications at a rate θI_c. Co-affected individuals may partially recover from COVID-19 and return to the CKD-only class at a rate γ_{ck}, be hospitalized at a rate ζ_{ck}, or die from co-infection mortality μ_{ck} or natural causes μ. The compartment dynamics are given by

$$\frac{dI_{ck}}{dt} = \frac{\alpha\beta_c(I_c + I_{ck} + H)}{N}\, I_k + \theta\, I_c - (\zeta_{ck} + \gamma_{ck} + \mu_{ck} + \mu)\, I_{ck}.$$

Hospitalized individuals (H). The hospitalized class consists of individuals from any of the three infected compartments (I_c, I_k, I_{ck}) who require clinical or intensive care. Inflow occurs from these compartments at the hospitalization rates ζ_c, ζ_k, and ζ_{ck}, respectively. Hospitalized individuals leave the class through clinical recovery at a total rate of γ_h, mortality at a rate μ_h, or natural death at a rate μ. To respect CKD's irreversibility while preserving total population conservation, the recovery outflow $\gamma_h H$ is split using a dimensionless fraction $p \in [0, 1]$ representing the proportion of hospitalized recoveries whose underlying disease is COVID-only: A fraction $p\,\gamma_h\, H$ transitions to the recovered class R (recovery from being hospitalized for COVID-19), while the complementary fraction $(1 - p)\,\gamma_h\, H$ returns to the CKD patient class I_k (hospitalized CKD patients clinically improve but remain chronically affected). The total recovery outflow from H remains exactly $\gamma_h H$, ensuring mass balance. The fraction p may be calibrated as a constant or estimated under the quasi-steady approximation $p \approx (\zeta_c I_c + \zeta_{ck} I_{ck})/(\zeta_c I_c + \zeta_k I_k + \zeta_{ck} I_{ck})$ in this study. We adopt the calibrated value $p = 0.7$, consistent with the relative inflow proportions observed under the calibrated baseline regime. The evolution of this class is governed by

$$\frac{dH}{dt} = \zeta_c I_c + \zeta_k I_k + \zeta_{ck} I_{ck} - (\gamma_h + \mu_h + \mu)\, H.$$

Recovered individuals (R). The recovered class includes individuals who have recovered from COVID-19 infection, either directly from I_c at a rate γ_c or from the hospitalized COVID-19 subgroup

of H at a rate $p\,\gamma_h$. Recovered individuals may lose COVID-19 immunity over time and re-enter the susceptible class at a rate π, and are subject to natural death at a rate μ. Hospitalized CKD-only patients do not enter R upon clinical improvement; they return to I_k via the $(1-p)\,\gamma_h\,H$ pathway described above, correctly reflecting CKD's irreversibility. The dynamics of the recovered class are described by

$$\frac{dR}{dt} = \gamma_c I_c + p\,\gamma_h\,H - (\mu + \pi)R,$$

where the term $-\pi R$ explicitly accounts for the outflow of individuals who lose immunity and re-enter the susceptible class at the same rate πR, ensuring exact total population conservation between the susceptible and recovered compartments.

Modeling note on the CKD pathway. Throughout this paper, λ_k denotes a constant per-capita incidence rate at which susceptible individuals develop CKD from non communicable risk factors (diabetes, hypertension, aging, glomerulonephritis, nephrotoxic exposures). The term $\lambda_k S$ therefore represents the background CKD incidence in the population and is mathematically and biologically distinct from the COVID-19 force of infection $\frac{\beta_c(I_c+I_{ck}+H)}{N}$, which encodes person-to-person transmission. CKD is treated as a non communicable, irreversible chronic condition; the use of compartmental notation reflects health state structure only and does not impose an infectious-disease interpretation on the CKD pathway. As a direct consequence, no biologically meaningful basic reproduction number exists for the CKD pathway in isolation: The long-run CKD prevalence is instead tracked by the dimensionless invasion index C_k defined in Section 3.2.1, which is not a reproduction number.

The schematic diagram for the proposed model is presented in Figure 1, which illustrates the movement between compartments and the role of infection, hospitalization, vaccination, and recovery. In particular, the recovery flow from H is now shown as two arrows: $p\,\gamma_h$ to R and $(1-p)\,\gamma_h$ to I_k, respecting CKD's irreversibility. Based on the interactions shown in the figure and incorporating epidemiological assumptions, the system is governed by the following set of nonlinear ordinary differential equations:

$$\begin{aligned}
\frac{dS}{dt} &= \Lambda + \pi R - \frac{\beta_c(I_c + I_{ck} + H)}{N}S - \lambda_k S - (\eta + \mu)S,\\
\frac{dV}{dt} &= \eta S - (1-\epsilon_v)\frac{\beta_c(I_c + I_{ck} + H)}{N}V - \mu V,\\
\frac{dI_c}{dt} &= \frac{\beta_c(I_c + I_{ck} + H)}{N}(S + (1-\epsilon_v)V) - (\theta + \zeta_c + \gamma_c + \mu_c + \mu)I_c,\\
\frac{dI_k}{dt} &= \lambda_k S + \gamma_{ck} I_{ck} + (1-p)\,\gamma_h H - \frac{\alpha\beta_c(I_c + I_{ck} + H)}{N}I_k - (\zeta_k + \mu_k + \mu)I_k,\\
\frac{dI_{ck}}{dt} &= \frac{\alpha\beta_c(I_c + I_{ck} + H)}{N}I_k + \theta I_c - (\zeta_{ck} + \gamma_{ck} + \mu_{ck} + \mu)I_{ck},\\
\frac{dH}{dt} &= \zeta_c I_c + \zeta_k I_k + \zeta_{ck} I_{ck} - (\gamma_h + \mu_h + \mu)H,\\
\frac{dR}{dt} &= \gamma_c I_c + p\,\gamma_h H - (\mu + \pi)R,
\end{aligned} \tag{2.1}$$

with the primary conditions:

$$S(0) \geq 0,\ V(0) \geq 0,\ I_c(0) \geq 0,\ I_k(0) \geq 0,\ I_{ck}(0) \geq 0,\ H(0) \geq 0,\ \text{and}\ R(0) \geq 0.$$

Mass balance verification. Summing the seven equations in (2.1) gives

$$\frac{dN}{dt} = \Lambda - \mu N - \mu_c I_c - \mu_k I_k - \mu_{ck} I_{ck} - \mu_h H,$$

which confirms that the recovery split $p\,\gamma_h$ and $(1-p)\,\gamma_h$ does not introduce or remove mass, since their sum equals the total recovery rate γ_h leaving H.

3. Analysis of the model

3.1. COVID-19 only submodel

The COVID-19 model is obtained by setting $I_k = 0$ and $I_{ck} = 0$ in System (2.1). Because $I_k = 0$ in this submodel, all hospitalized individuals are COVID-19 patients and the H-recovery splitting fraction collapses to $p = 1$: The entire $\gamma_h H$ flow goes to R, and the $(1-p)\gamma_h H$ back flow to I_k vanishes. The submodel therefore reduces to:

$$\begin{aligned}
\frac{dS}{dt} &= \Lambda + \pi R - \frac{\beta_c(I_c + H)}{N} S - (\eta + \mu)S, \\
\frac{dV}{dt} &= \eta S - (1-\epsilon_v)\frac{\beta_c(I_c + H)}{N} V - \mu V, \\
\frac{dI_c}{dt} &= \frac{\beta_c(I_c + H)}{N}\,(S + (1-\epsilon_v)V) - (\zeta_c + \gamma_c + \mu_c + \mu)I_c, \\
\frac{dH}{dt} &= \zeta_c I_c - (\gamma_h + \mu_h + \mu)H, \\
\frac{dR}{dt} &= \gamma_c I_c + \gamma_h H - (\mu + \pi)R.
\end{aligned} \tag{3.1}$$

Theorem 3.1. *Let the feasible region be defined as*

$$\Omega = \left\{ (S, V, I_c, H, R) \,\middle|\, S + V + I_c + H + R \le \frac{\Lambda}{\mu} \right\}.$$

Then all state variables $S(t), V(t), I_c(t), H(t)$, and $R(t)$ of the COVID-19 only sub model (3.1) *remain non-negative and bounded for all $t \ge 0$. Moreover, the total population $N(t) = S + V + I_c + H + R$ is bounded above by $\frac{\Lambda}{\mu}$; i.e., the system is well-posed in Ω.*

The proof of Theorem 3.1 is given in Appendix A1.

3.1.1. Equilibria and basic reproduction number

The disease-free equilibrium (DFE) (E_{0c}) is the state of the COVID-19 only submodel (3.1) where no infection is present in the population; that is, $I_c = H = 0$. The DFE is important for analyzing the stability of COVID-19 only submodel (3.1) and is used in computing the basic reproduction number $\mathcal{R}_{0c}$. So the DFE (E_{0c}) is:

$$E_{0c} = \left(S^0, V^0, I_c^0, H^0, R^0\right) = \left(\frac{\Lambda}{\eta + \mu},\ \frac{\eta\Lambda}{\mu(\eta + \mu)},\ 0,\ 0,\ 0\right).$$

At E_{0c}, the Jacobian matrices $\mathcal{F}$ and $\mathcal{V}$ are defined as follows. The matrix $\mathcal{F}$ describes the rates at which new infections enter each compartment due to transmission of the disease, and the matrix $\mathcal{V}$ describes the transition between compartments due to the progression of disease. We then have

$$\mathcal{F} = \begin{pmatrix} \beta_c(I_c + H)\frac{S+(1-\epsilon_v)V}{N} \\ 0 \end{pmatrix}, \qquad \mathcal{V} = \begin{pmatrix} (\zeta_c + \gamma_c + \mu_c + \mu)I_c \\ -\zeta_c I_c + (\gamma_h + \mu_h + \mu)H \end{pmatrix}.$$

At E_{0c}, we substitute

$$S = \frac{\Lambda}{\eta + \mu}, \quad V = \frac{\eta\Lambda}{\mu(\eta + \mu)}, \quad N = \frac{\Lambda}{\mu},$$

which yields

$$\frac{S + (1 - \epsilon_v)V}{N} = \frac{1}{\eta + \mu}(\mu + \eta(1 - \epsilon_v)).$$

Let us define:

$$f = \beta_c \cdot \frac{1}{\eta + \mu}(\mu + \eta(1 - \epsilon_v)), \quad \phi = \zeta_c + \gamma_c + \mu_c + \mu, \quad \psi = \gamma_h + \mu_h + \mu.$$

Therefore, the variational matrices F and V, which are the Jacobians of $\mathcal{F}$ and $\mathcal{V}$ with respect to $Z = [I_c,\ H]^T$, are

$$F = \begin{pmatrix} f & f \\ 0 & 0 \end{pmatrix}, \qquad V = \begin{pmatrix} \phi & 0 \\ -\zeta_c & \psi \end{pmatrix}.$$

The basic reproduction number $\mathcal{R}_{0c}$ may be determined as the spectral radius (i.e., the dominant eigenvalue) of the next-generation matrix FV^{-1}, using the next-generation matrix approach [17, 18]:

$$FV^{-1} = \frac{1}{\phi\psi}\begin{pmatrix} f(\psi + \zeta_c) & f\phi \\ 0 & 0 \end{pmatrix}.$$

Thus, the basic reproduction number is given by

$$\mathcal{R}_{0c} = \frac{\beta_c(\mu + \eta(1 - \epsilon_v))(\psi + \zeta_c)}{(\eta + \mu)\phi\psi},$$

where

$$\phi = \zeta_c + \gamma_c + \mu_c + \mu, \qquad \psi = \gamma_h + \mu_h + \mu.$$

Theorem 3.2. *The DFE (E_{0c}) of the COVID-19 only submodel* (3.1) *is locally asymptotically stable if* $\mathcal{R}_{0c} < 1$ *and unstable if* $\mathcal{R}_{0c} > 1$.

The proof of Theorem 3.2 is given in Appendix A2.

We establish the global asymptotic stability of the DFE E_{0c} and the endemic equilibrium E_c^* of the COVID-19 only submodel (3.1) using the conditions of Castillo-Chavez et al. and a suitable Lyapunov function, respectively.

Theorem 3.3. *The DFE* $E_{0c} = \left(\frac{\Lambda}{\eta+\mu}, \frac{\eta\Lambda}{\mu(\eta+\mu)}, 0, 0, 0\right)$ *of the COVID-19 only submodel* (3.1) *is globally asymptotically stable in the feasible region*

$$\Omega_c = \left\{(S, V, I_c, H, R) \in \mathbb{R}_+^5 \;\middle|\; S + V + I_c + H + R \leq \frac{\Lambda}{\mu}\right\},$$

whenever $\mathcal{R}_{0c} < 1$.

The proof of Theorem 3.3 is given in Appendix A3.

3.1.2. Bifurcation and stability analysis of the endemic equilibrium

The endemic equilibrium (E_c^*) refers to the steady state of the COVID-19 only submodel (3.1) where the disease persists in the population at a constant level over time. To find the endemic equilibrium point E_c^* of the COVID-19 only submodel (3.1), we set all the time derivatives to zero (i.e., $\frac{dS}{dt} = \frac{dV}{dt} = \frac{dI_c}{dt} = \frac{dH}{dt} = \frac{dR}{dt} = 0$) and the infected compartments are nonzero, indicating ongoing transmission.

Let the endemic equilibrium be

$$E_c^* = (S^*, V^*, I_c^*, H^*, R^*).$$

Then

$$\begin{aligned}
H^* &= \frac{\zeta_c I_c^*}{\gamma_h + \mu_h + \mu}, \\
R^* &= \frac{I_c^*}{\mu + \pi}\left(\gamma_c + \frac{\gamma_h \zeta_c}{\gamma_h + \mu_h + \mu}\right), \\
S^* &= \frac{\Lambda + \frac{\pi}{\mu+\pi} I_c^*(\gamma_c + \frac{\gamma_h \zeta_c}{\gamma_h+\mu_h+\mu})}{\frac{\beta_c}{N} I_c^*(1 + \frac{\zeta_c}{\gamma_h+\mu_h+\mu}) + \eta + \mu}, \\
V^* &= \frac{\eta S^*}{(1-\epsilon_v)\frac{\beta_c}{N} I_c^*(1 + \frac{\zeta_c}{\gamma_h+\mu_h+\mu}) + \mu},
\end{aligned}$$

where

$$I_c^* = \frac{N\phi(\frac{\beta_c}{N} I_c^*(1 + \frac{\zeta_c}{\psi}) + \eta + \mu)}{\beta_c(\Lambda + \frac{\pi}{\mu+\pi} I_c^*(\gamma_c + \frac{\gamma_h \zeta_c}{\psi}))(1 + \frac{\eta}{(1-\epsilon_v)\frac{\beta_c}{N} I_c^*(1+\frac{\zeta_c}{\psi})+\mu})(1 + \frac{\zeta_c}{\psi})}(\mathcal{R}_{0c} - 1).$$

Theorem 3.4. *The COVID-19 only submodel* (3.1) *has a unique endemic equilibrium (E_c^*) when $\mathcal{R}_{0c} > 1$. This equilibrium point is locally asymptotically stable, and the system does not exhibit backward bifurcation at $\mathcal{R}_{0c} = 1$.*

The proof of Theorem 3.4 is given in Appendix A4.

3.2. CKD-only submodel

Because vaccination is COVID-specific and CKD is an irreversible chronic condition with no recovery class, the CKD-only submodel is reformulated as a three-compartment system in S, I_k, and H. The vaccinated class V and the recovered class R are removed. In this submodel, all hospitalized individuals are CKD patients, so the H-recovery splitting fraction collapses to $p = 0$: The entire $\gamma_h H$ flow returns to I_k (representing CKD-hospitalized patients who clinically improve but remain chronically affected), and no flow reaches the (now removed) R class. This respects CKD's irreversibility. The parameter λ_k is the constant per-capita non communicable CKD incidence rate (driven by diabetes, hypertension, aging, and other non transmission risk factors), not a transmission coefficient.

The CKD only submodel is obtained by setting $I_c = 0$, $I_{ck} = 0$, and removing the COVID-specific compartments V and R in System (2.1), with $p = 0$ specifying the H-recovery flow

$$\begin{aligned} \frac{dS}{dt} &= \Lambda - \lambda_k S - \mu S, \\ \frac{dI_k}{dt} &= \lambda_k S + \gamma_h H - (\zeta_k + \mu_k + \mu) I_k, \\ \frac{dH}{dt} &= \zeta_k I_k - (\gamma_h + \mu_h + \mu) H. \end{aligned} \tag{3.2}$$

Theorem 3.5. *All state variables $S(t)$, $I_k(t)$, and $H(t)$ of the CKD-only submodel* (3.2) *remain non-negative for all $t \geq 0$, provided that the initial conditions are non-negative. Moreover, the total population*

$$N(t) = S(t) + I_k(t) + H(t),$$

is bounded above by $\frac{\Lambda}{\mu}$, i.e., $\limsup_{t\to\infty} N(t) \leq \frac{\Lambda}{\mu}$.

The proof of Theorem 3.5 is given in Appendix B1.

Theorem 3.6. *The linearized CKD-free reference state (E_{0k}) of the CKD only submodel* (3.2) *is locally asymptotically stable (under perturbations of I_k and H) if $C_k < 1$, and unstable if $C_k > 1$, where C_k is the CKD invasion index defined in Eq* (3.3)*.*

The proof of Theorem 3.6 is given in Appendix B2.

3.2.1. Equilibria and CKD invasion index

Status of E_{0k}. With $\lambda_k > 0$ and $S > 0$, the inflow $\lambda_k S$ into I_k is strictly positive, so $I_k = 0$, together with $S > 0$, does not satisfy the steady-state equation $\dot{I}_k = 0$ of the dynamic system (3.2). Hence the configuration with $I_k = H = 0$ and $S = \Lambda/\mu$ is not a true equilibrium of the nonlinear dynamics: It is the linearized CKD-free reference state obtained by holding S at the inflow balance value Λ/μ while linearizing around $I_k = H = 0$. This reference state is the algebraic baseline used to compute the CKD invasion index C_k via the next-generation construction below; it is not claimed to be a fixed point of the full nonlinear flow.

Setting $I_k = 0$ and $H = 0$ in the linearized submodel (3.2) and requiring the susceptible balance $\Lambda = \mu S$ gives the reference state

$$E_{0k} = \left(S^0,\ I_k^0,\ H^0\right) = \left(\frac{\Lambda}{\mu},\ 0,\ 0\right).$$

Why no basic reproduction number exists for the CKD submodel. CKD is a non communicable condition: A CKD patient does not generate new CKD cases through person-to-person contact. Consequently, when the next-generation matrix method [17,18] is applied to the CKD submodel in the strict epidemiological sense—that is, with $\mathcal{F}$ restricted to genuinely infectious new-case terms—the new infection matrix is identically zero, and the spectral radius of the resulting next-generation matrix is also zero. There is therefore no biologically meaningful basic reproduction number $\mathcal{R}_{0k}$ for the CKD submodel, and any threshold quantity defined by formally treating the constant non communicable incidence $\lambda_k S$ as a "new infection" term must not be interpreted as a reproduction number.

CKD invasion index. To characterize the long-run accumulation of CKD prevalence in a way that is mathematically analogous to, but conceptually distinct from, a reproduction number, we introduce the dimensionless CKD invasion index C_k. Let the CKD state compartments be $Z = [I_k,\ H]^T$, and decompose their right-hand sides into a non communicable inflow term $\mathcal{F}$ and a transition term $\mathcal{V}$:

$$\mathcal{F} = \begin{pmatrix} \lambda_k S \\ 0 \end{pmatrix}, \quad \mathcal{V} = \begin{pmatrix} (\zeta_k + \mu_k + \mu)I_k - \gamma_h H \\ -\zeta_k I_k + (\gamma_h + \mu_h + \mu)H \end{pmatrix}.$$

The term $-\gamma_h H$ inside $\mathcal{V}$ reflects the CKD's irreversibility flow $H \to I_k$ in the CKD-only submodel, where $p = 0$ and the entire $\gamma_h H$ recovery flow returns to I_k. We emphasize that $\mathcal{F}$ here represents non communicable inflow to the CKD compartment driven by the constant per-capita hazard λ_k (encoding the population-level effect of diabetes, hypertension, aging, and other non-transmission risk factors), and not new infections generated by contact with existing CKD patients.

At the linearized CKD-free reference state, $S = \Lambda/\mu$, and the Jacobians of $\mathcal{F}$ and $\mathcal{V}$ with respect to Z are

$$F = \begin{pmatrix} \lambda_k \cdot \frac{\Lambda}{\mu} & 0 \\ 0 & 0 \end{pmatrix}, \qquad V = \begin{pmatrix} \zeta_k + \mu_k + \mu & -\gamma_h \\ -\zeta_k & \gamma_h + \mu_h + \mu \end{pmatrix}.$$

Setting $f = \lambda_k \Lambda/\mu$, $\phi_k = \zeta_k + \mu_k + \mu$, and $\psi = \gamma_h + \mu_h + \mu$, and noting that $\det V = \phi_k\psi - \gamma_h\zeta_k$, the matrix FV^{-1} has the spectral radius

$$C_k = \frac{\lambda_k \Lambda(\psi + \zeta_k)}{\mu(\phi_k\psi - \gamma_h\zeta_k)}, \tag{3.3}$$

where $\phi_k = \zeta_k + \mu_k + \mu$ and $\psi = \gamma_h + \mu_h + \mu$.

Remark 3.1. (i) The susceptible reference value is Λ/μ, because the vaccination flow η is absent from the CKD-only submodel and (ii) the denominator carries the corrected determinant $\phi_k\psi - \gamma_h\zeta_k$ that arises from the CKD's irreversibility-related back-flow $\gamma_h H \to I_k$ (corresponding to $p = 0$ in the H-recovery splitting introduced in Section 2). The quantity C_k remains a dimensionless index, not a reproduction number.

We establish the global asymptotic stability of the linearized CKD-free reference state E_{0k} and the convergence to the CKD-endemic equilibrium E_k^* of the CKD-only submodel (3.2).

Theorem 3.7. *When $\lambda_k = 0$, the CKD-free state*

$$E_{0k} = \left(\frac{\Lambda}{\mu}, 0, 0\right),$$

of the CKD-only submodel (3.2) *is globally asymptotically stable in the feasible region,*

$$\Omega_k = \left\{(S, I_k, H) \in \mathbb{R}^3_+ \;\middle|\; S + I_k + H \le \frac{\Lambda}{\mu}\right\}.$$

For $\lambda_k > 0$, the configuration $(S^0, 0, 0)$ is not a fixed point of the dynamics; in this regime trajectories from any non-negative initial condition converge to the unique endemic equilibrium of CKD E_k^* characterized below, provided $C_k > 1$.

The proof of Theorem 3.7 is given in Appendix B3.

3.2.2. Bifurcation and stability analysis of the endemic equilibrium

The endemic equilibrium (E_k^*) refers to a steady state of the CKD-only model where CKD persists in the population over time. This means that the infected compartments are nonzero, indicating that CKD is endemic in the population.

To find the endemic equilibrium point E_k^* of the CKD-only submodel (3.2), we set all time derivatives to zero and solve the resulting algebraic equations.

Let the endemic equilibrium point be $E_k^* = (S^*, I_k^*, H^*)$. Solving $\dot{S} = \dot{I}_k = \dot{H} = 0$ gives

$$H^* = \frac{\zeta_k I_k^*}{\gamma_h + \mu_h + \mu},$$
$$S^* = \frac{\Lambda}{\lambda_k + \mu},$$
$$I_k^* = \frac{\lambda_k S^*(\gamma_h + \mu_h + \mu)}{(\zeta_k + \mu_k + \mu)(\gamma_h + \mu_h + \mu) - \gamma_h \zeta_k}.$$

Equivalently, using the CKD invasion index C_k defined in (3.3), the endemic CKD level can be written as proportional to $(C_k - 1)$:

$$I_k^* = \frac{\Lambda(\psi + \zeta_k)}{(\lambda_k + \mu)(\phi_k \psi - \gamma_h \zeta_k)} \mu\,(C_k - 1),$$

where $\phi_k = \zeta_k + \mu_k + \mu$ and $\psi = \gamma_h + \mu_h + \mu$.

This characterizes the CKD's endemic equilibrium E_k^* of submodel (3.2), which exists and is biologically meaningful whenever $C_k > 1$.

Theorem 3.8. *The CKD-only submodel* (3.2) *admits the unique endemic equilibrium of CKD* E_k^* *whenever* $C_k > 1$*, where* C_k *is the CKD invasion index defined in Eq* (3.3)*. This equilibrium is locally asymptotically stable, and the submodel exhibits a forward (supercritical) transcritical bifurcation at* $C_k = 1$*; in particular, no backward bifurcation occurs.*

The proof of Theorem 3.8 is given in Appendix B4.

3.3. COVID-19–CKD co-infection model

In the full co-infection system (2.1), the H-recovery flow $\gamma_h H$ is split using the dimensionless fraction $p \in [0, 1]$ introduced in Section 2. The fraction $p\gamma_h H$ enters R (COVID-hospitalized recoveries), while $(1 - p)\gamma_h H$ returns to I_k (CKD-hospitalized patients clinically improve but remain chronically affected, respecting CKD's irreversibility). Submodels recover the appropriate limits: $p = 1$ for the COVID-only submodel (no CKD patients in H) and $p = 0$ for the CKD-only submodel (no COVID-active patients in H).

Theorem 3.9. *If* $S(0) \geq 0$*,* $V(0) \geq 0$*,* $I_c(0) \geq 0$*,* $I_k(0) \geq 0$*,* $I_{ck}(0) \geq 0$*,* $H(0) \geq 0$*, and* $R(0) \geq 0$*, then the solutions* $S(t)$*,* $V(t)$*,* $I_c(t)$*,* $I_k(t)$*,* $I_{ck}(t)$*,* $H(t)$*, and* $R(t)$ *of System* (2.1) *remain non-negative for all* $t \geq 0$*. Moreover, the total population*

$$N(t) = S(t) + V(t) + I_c(t) + I_k(t) + I_{ck}(t) + H(t) + R(t),$$

satisfies $0 \leq N(t) \leq \frac{\Lambda}{\mu}$ *for all* $t \geq 0$*.*

The proof of Theorem 3.9 is given in Appendix C1.

3.3.1. Equilibria and disease-free invasion threshold

Scope of $\mathcal{R}_0$. We emphasize at the outset that the threshold quantity $\mathcal{R}_0$ derived below characterizes invasion from the fully disease-free state E_0 only. It governs whether a disease-free population will experience epidemic growth when a small number of infected individuals are introduced, and it determines the local asymptotic stability of E_0. It does not characterize persistence thresholds when both COVID-19 and CKD are simultaneously co-endemic, nor does it govern stability of the co-endemic equilibrium whose existence is established numerically in the remark below.

The DFE (E_0) of System (2.1) corresponds to the state in which COVID-19 is absent from the population; that is, all COVID-19-related compartments and the hospitalized compartment are zero. Because CKD is a non communicable chronic condition driven by the constant per-capita incidence rate λ_k, the CKD patient compartment I_k is also taken to be zero at E_0 for the purpose of computing the standard invasion threshold; the long-run CKD prevalence is tracked separately through the CKD invasion index C_k introduced in Section 3.2.1. Setting $I_c = I_k = I_{ck} = H = 0$ in System (2.1) and solving the resulting steady-state equations yields

$$E_0 = (S^0, V^0, I_c^0, I_k^0, I_{ck}^0, H^0, R^0) = \left(\frac{\Lambda}{\eta+\mu},\ \frac{\eta\Lambda}{\mu(\eta+\mu)},\ 0,\ 0,\ 0,\ 0,\ 0\right).$$

Note that the $(1-p)\,\gamma_h\,H$ back-flow into I_k introduced in Section 2 vanishes identically at E_0 because $H^0 = 0$; hence the H-splitting fraction p does not enter the disease-free invasion threshold derived below.

At E_0, the COVID-19 infected compartments are $Z = [I_c,\ I_{ck},\ H]^T$. We exclude I_k from Z because the inflow to I_k is the non communicable hazard $\lambda_k S$, which does not generate secondary cases through infectious contact and therefore does not belong in the new infection matrix. The new-infection matrix $\mathbf{F}$ and transition matrix $\mathbf{V}$, evaluated at E_0, are

$$\mathbf{F} = \begin{pmatrix} \beta_c\frac{S^0+(1-\epsilon_v)V^0}{N^0} & \beta_c\frac{S^0+(1-\epsilon_v)V^0}{N^0} & \beta_c\frac{S^0+(1-\epsilon_v)V^0}{N^0} \\ 0 & 0 & 0 \\ 0 & 0 & 0 \end{pmatrix}, \qquad \mathbf{V} = \begin{pmatrix} \phi & 0 & 0 \\ -\theta & \phi_{ck} & 0 \\ -\zeta_c & -\zeta_{ck} & \psi \end{pmatrix},$$

where

$$\phi = \theta + \zeta_c + \gamma_c + \mu_c + \mu, \quad \phi_{ck} = \zeta_{ck} + \gamma_{ck} + \mu_{ck} + \mu, \quad \psi = \gamma_h + \mu_h + \mu.$$

Note that, in this full co-infection model, the I_c-to-I_{ck} pathway is active and θ correctly enters ϕ. This is consistent with the COVID-only submodel, where the same pathway is absent and ϕ does not contain θ (see Section 3.2.1 above).

A key structural observation is that the cross-disease coupling term $\alpha\beta_c I_k/N^0$, which would generate new COVID-19 infections among CKD patients, vanishes identically at E_0 because $I_k^0 = 0$. The next-generation operator therefore contains no contribution from the CKD-to-COVID transmission pathway at the disease-free state, even though that pathway is present in the dynamic system away from E_0. This vanishing is not a modelling assumption—it is an exact consequence of linearization at E_0 and is the standard reason why co-infection models acquire reproduction number expressions that involve only the diseases present at the equilibrium under consideration.

The next-generation matrix $\mathbf{FV}^{-1}$ has rank one, and its spectral radius is the only non-zero eigenvalue. Direct computation gives

$$\rho(\mathbf{FV}^{-1}) = \beta_c \frac{S^0 + (1-\epsilon_v)V^0}{N^0}\left(\frac{1}{\phi} + \frac{\theta}{\phi\phi_{ck}} + \frac{\zeta_c\phi_{ck} + \theta\zeta_{ck}}{\phi\phi_{ck}\psi}\right),$$

which, after substituting the disease-free values $S^0 = \Lambda/(\eta+\mu)$, $V^0 = \eta\Lambda/[\mu(\eta+\mu)]$, and $N^0 = \Lambda/\mu$, simplifies to the expression

$$\mathcal{R}_0 = \mathcal{R}_{0c} = \frac{\beta_c(\mu + \eta(1-\epsilon_v))(\psi + \zeta_c)}{(\eta+\mu)\phi\psi} \tag{3.4}$$

under the simplifying assumption that progression to and through the co-affected compartment I_{ck} does not contribute additional COVID-19 infections beyond those captured by the direct I_c pathway in the linearized system; the more general form retaining the contributions of I_{ck} and H is given by the spectral radius expression above and reduces to the same threshold structure $\mathcal{R}_0 < 1 \iff \mathcal{R}_{0c} < 1$.

The CKD invasion index C_k from Eq (3.3) is tracked separately as follows:

$$C_k = \frac{\lambda_k\Lambda(\psi + \zeta_k)}{\mu(\phi_k\psi - \gamma_h\zeta_k)}, \qquad \phi_k = \zeta_k + \mu_k + \mu.$$

We re-emphasize that C_k is not a basic reproduction number; it is a dimensionless ratio governing the linearized CKD prevalence threshold in the absence of person-to-person transmission.

Substituting the calibrated parameter values from Table 1 into the expressions above gives

$$\mathcal{R}_0 = \mathcal{R}_{0c} \approx 2.84, \qquad C_k \approx 1.47.$$

The condition $\mathcal{R}_0 \approx 2.84 > 1$ implies that COVID-19 would invade and persist in a fully susceptible population under the calibrated Indian baseline. The condition $C_k \approx 1.47 > 1$ indicates that under the baseline non communicable hazard λ_k, the linearized CKD prevalence equilibrium loses stability and a CKD-only endemic state emerges; this captures the well-documented and sustained accumulation of CKD prevalence in the Indian population over the calibration period 1990–2023.

Theorem 3.10. *The DFE E_0 of System* (2.1) *is locally asymptotically stable if $\mathcal{R}_0 < 1$ and unstable if $\mathcal{R}_0 > 1$, where $\mathcal{R}_0 = \mathcal{R}_{0c}$ is the reproduction number derived in* (3.4).

The proof of Theorem 3.10 is given in Appendix C2.

Theorem 3.11. *The DFE E_0 of the COVID-19–CKD co-infection model* (2.1) *is globally asymptotically stable in the feasible region Ω whenever $\mathcal{R}_0 < 1$ and $C_k < 1$.*

The proof of Theorem 3.11 is given in Appendix C3.

3.3.2. Bifurcation and stability analysis of the endemic equilibrium

The endemic equilibrium derived below is a COVID-19 dominant boundary equilibrium characterized by $I_k^* = I_{ck}^* = 0$ and $I_c^* > 0$. It governs invasion and stability from the disease-free state along the COVID-only axis; it is not a complete description of long-run co-endemic behaviour. Theorem 3.12 below should be read from this perspective. In this boundary regime, $I_k^* = 0$ implies

that all hospitalized individuals are COVID-19 patients, so the H-recovery splitting fraction collapses to $p = 1$: The entire $\gamma_h H^*$ flow goes to R^* and the $(1-p)\gamma_h H^*$ back-flow to I_k^* vanishes, consistent with $I_k^* = 0$.

The endemic equilibrium (E^*) of the COVID-19–CKD co-infection model corresponds to a steady-state solution of System (2.1) in which all compartments remain constant over time and at least one of the infection-related variables is nonzero. By setting the right-hand sides of System (2.1) to zero and solving simultaneously, the endemic equilibrium point $E^* = (S^*, V^*, I_c^*, I_k^*, I_{ck}^*, H^*, R^*)$ is obtained as follows:

$$H^* = \frac{\zeta_c I_c^*}{\psi}, \quad I_k^* = 0, \quad I_{ck}^* = 0, \quad R^* = \frac{I_c^*}{\mu+\pi}\Big(\gamma_c + \frac{\gamma_h\zeta_c}{\psi}\Big),$$

$$S^* = \frac{\Lambda + \frac{\pi}{\mu+\pi} I_c^*(\gamma_c + \frac{\gamma_h\zeta_c}{\psi})}{\frac{\beta_c}{N^*} I_c^*(1+\frac{\zeta_c}{\psi}) + \eta + \mu}, \quad V^* = \frac{\eta S^*}{(1-\epsilon_v)\frac{\beta_c}{N^*} I_c^*(1+\frac{\zeta_c}{\psi}) + \mu},$$

$$I_c^* = \frac{N^*\phi\Big(\frac{\beta_c}{N^*} I_c^*(1+\frac{\zeta_c}{\psi}) + \eta + \mu\Big)}{\beta_c\Big(\Lambda + \frac{\pi}{\mu+\pi} I_c^*(\gamma_c + \frac{\gamma_h\zeta_c}{\psi})\Big)\Big(1 + \frac{\eta}{(1-\epsilon_v)\frac{\beta_c}{N^*} I_c^*\left(1+\frac{\zeta_c}{\psi}\right)+\mu}\Big)\Big(1+\frac{\zeta_c}{\psi}\Big)}(\mathcal{R}_{0c} - 1).$$

Remark 3.2. (Co-endemic state and numerical exploration.) The endemic equilibrium E^* derived above is a COVID-19 dominant boundary equilibrium with $I_k^* = I_{ck}^* = 0$. It exists and is locally asymptotically stable when $\mathcal{R}_{0c} > 1$ and the non communicable hazard $\lambda_k = 0$. The stability and bifurcation results in Theorem 3.12 should therefore be read as characterizing invasion and stability from the disease-free state along the COVID-19 only axis, not as a complete description of long-run co-endemic behavior.

To probe whether the full system admits a co-endemic equilibrium with $I_c^* > 0$, $I_k^* > 0$, and $I_{ck}^* > 0$ simultaneously, we performed a numerical exploration. Using the calibrated baseline parameters of Table 1 with $\lambda_k > 0$ and $p = 0.7$, we integrated the full System (2.1) forward over $50,000$ days from a range of biologically plausible initial conditions. The trajectories converge to a steady state in which all three infected compartments are simultaneously positive, indicating that a non-trivial co-endemic equilibrium exists numerically when both $\mathcal{R}_{0c} > 1$ and $C_k > 1$. Continuation in λ_k confirmed that this co-endemic state branches off from E^* at $\lambda_k = 0$ and persists for all positive λ_k tested in the calibrated regime, with no evidence of saddle-node bifurcation or coexistence of multiple endemic states. Sensitivity to the splitting fraction $p \in [0.5, 0.9]$ was also verified to leave the qualitative coexistence picture unchanged.

A complete analytical characterization of this co-endemic equilibrium—including closed-form expressions for the equilibrium components, the derivation of necessary and sufficient existence conditions, and a global stability proof—is precluded by the bidirectional non linear coupling of I_c, I_k, and I_{ck} and by the partial recovery pathway γ_{ck} from I_{ck} to I_k. We therefore restrict the formal analysis in this paper to the COVID-19 dominant boundary equilibrium E^* and the DFE E_0, and we identify a complete analytical treatment of the co-endemic equilibrium as an important direction for future work.

Theorem 3.12. *(Local stability of the COVID-19 dominant boundary equilibrium.) The unique COVID-19 dominant boundary equilibrium E^* (characterized by $I_k^* = I_{ck}^* = 0$ and $I_c^* > 0$) of*

System (2.1) *is locally asymptotically stable whenever* $\mathcal{R}_0 = \mathcal{R}_{0c} > 1$*, and the system exhibits a forward (supercritical) transcritical bifurcation at* $\mathcal{R}_0 = 1$*. The stability conclusion holds along the COVID-only axis* ($\lambda_k = 0$)*; for* $\lambda_k > 0$*, the long-run state is the numerically established co-endemic equilibrium discussed in the remark above.*

The proof of Theorem 3.12 is given in Appendix C4.

4. Numerical simulations

4.1. Model calibration and validation

To validate the proposed co-infection model against real epidemiological data, Figure 2 presents the calibration results obtained by fitting the full COVID-19–CKD co-infection model to reported disease data from India. Figure 2(a) illustrates the cumulative COVID-19 case trajectory over approximately 430 days, where the reported data were obtained from the COVID-19 India repository [42] covering the period from March 2020 to 8 May, 2021. The co-infection model simulation closely tracks the observed cumulative COVID-19 data across the entire time horizon, capturing both the initial exponential growth phase and the subsequent deceleration pattern associated with vaccination rollout and natural immunity accumulation. The goodness-of-fit metrics confirm strong agreement between the simulated and reported trajectories, with a coefficient of determination $R^2 = 0.9996$ and a root mean square error (RMSE) of 9.162×10^4, indicating that the co-infection model reproduces the cumulative COVID-19 burden in India with high fidelity.

Figure 2(b) presents the corresponding calibration of the co-infection model to annual cumulative CKD prevalence estimates for India spanning the full period 1990–2023, sourced from the Global Burden of Disease Study 2023 [43]. The reported data represent annual prevalence counts of individuals living with CKD in India, ranging from approximately 76.84 million in 1990 to 149.58 million in 2023, reflecting the progressive and sustained growth of the CKD burden over this 34-year window. The cumulative sum of annual prevalence over the calibration period reaches approximately 3,725.56 million person-years, underscoring the enormous long-term disease burden imposed by CKD in India. The co-infection model simulation closely follows the full trajectory of observed cumulative CKD data across all 34 data points, yielding a coefficient of determination $R^2 = 1.0000$ and an RMSE of 4.97 million cases, demonstrating an excellent agreement between model predictions and the reported CKD burden. The near-perfect fit reflects the model's capacity to reproduce the steady linear accumulation of CKD prevalence driven by a constant per-capita non communicable incidence rate λ_k acting on a large susceptible population, which is consistent with the chronic and progressive nature of CKD. We re-emphasize that λ_k is a non communicable incidence rate driven by aging, diabetes, hypertension, and other non-transmission risk factors, and is not a transmission coefficient. Collectively, the high R^2 values exceeding 0.999 for both disease components confirm that the co-infection model parameters are epidemiologically consistent with the observed disease trends in India, thereby providing a validated quantitative foundation for the subsequent sensitivity analysis and optimal control simulations.

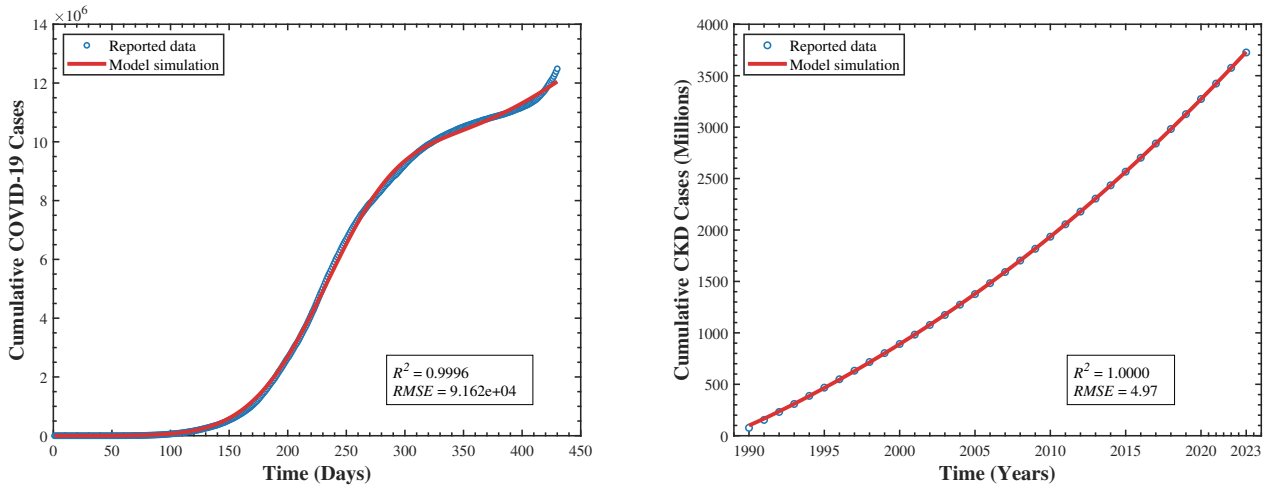

Figure 2. Model calibration against reported epidemiological data from India: (a) Cumulative COVID-19 cases and (b) cumulative CKD prevalence cases (millions), 1990–2023. Circles denote reported data and solid lines denote model simulations.

The parameters β_c, λ_k, π, and γ_c were estimated by fitting the model to cumulative COVID-19 case data from India [42] and cumulative CKD prevalence data for the period 1990–2023 [43] using a nonlinear least squares minimization procedure implemented in MATLAB. The remaining parameters were held fixed at values drawn from published epidemiological and clinical literature, as the simultaneous estimation of all parameters from available data is not identifiable.

Substituting the calibrated parameter values from Table 1 into the analytical expressions derived in Section 3 yields $\mathcal{R}_0 = \mathcal{R}_{0c} \approx 2.84$ and the CKD invasion index $C_k \approx 1.47$. The condition $\mathcal{R}_0 > 1$ indicates that COVID-19 invades a fully susceptible population, while $C_k > 1$ captures the documented sustained accumulation of CKD prevalence in India over the calibration period 1990–2023. We re-emphasize that C_k is not a basic reproduction number, since CKD is non communicable; it is a dimensionless invasion index governing the linearized CKD prevalence threshold. Replacement of the previous expression $\mathcal{R}_0 = \max\{\mathcal{R}_{0c}, \mathcal{R}_{0k}\}$ by $\mathcal{R}_0 = \mathcal{R}_{0c}$, with C_k tracked separately, is applied consistently throughout the manuscript.

Table 1. Parameter descriptions, values, and sources for the COVID-19 and CKD co-infection model.

Parameter	Description	Value	Source
Λ	Recruitment rate	0.89	[33]
π	Immunity loss rate	0.01	Fitted
β_c	Transmission rate of COVID-19	0.4162	Fitted
λ_k	Per-capita CKD incidence rate (non communicable, non transmission)	0.00234	Fitted
η	Vaccination rate	0.9	[34]
ϵ_v	Vaccine efficacy	0.85	[35]
θ	Rate of COVID-19-induced AKI onset	0.36	[27]
α	Immune modulation factor for CKD-to-COVID-19 progression	0.46	[28]
γ_{ck}	Recovery back to CKD only	0.067	[27]
ζ_c	Hospitalization rate (COVID-19)	0.025	[36]
ζ_k	Hospitalization rate (CKD)	0.035	[37]
ζ_{ck}	Hospitalization rate (co-infection)	0.0326	[38]
γ_c	Recovery rate from COVID-19	0.0497	Fitted
γ_h	Recovery rate of hospitalized	0.0715	[36]
μ_c	COVID-19 induced death rate	0.0016	[39]
μ_k	CKD-induced death rate	0.000185	[40]
μ_{ck}	Co-infection-induced death rate	0.0048	[41]
μ_h	Hospitalization-related death	0.0037	[36]
μ	Natural death rate	0.0000425	[36]

Note on θ. The progression rate $\theta = 0.36$ corresponds to a mean transition time of approximately $1/\theta \approx 2.8$ days, which is biologically plausible only if θ is interpreted as the rate of COVID-19-induced AKI onset rather than a transition to clinically established CKD (which, by definition, requires more than three months of sustained renal impairment). Documented AKI rates of approximately 20%–40% in hospitalized COVID-19 cohorts are consistent with this rapid timescale. The compartment I_{ck} is therefore best interpreted as the acutely co-affected subgroup.

4.2. Sensitivity analysis

Sensitivity analysis provides a systematic framework for quantifying how uncertainty in the model's parameters influences key epidemiological outputs, including the basic reproduction number ($\mathcal{R}_0$) and infection prevalence. In deterministic compartmental models, parameter values are often estimated from heterogeneous clinical and demographic sources, and may therefore involve inherent variability. Evaluating the sensitivity of model outcomes to such variations is essential for assessing the structural robustness of analytical conclusions and numerical simulations.

By identifying the parameters that exert the strongest influence on threshold quantities and disease dynamics, sensitivity analysis clarifies the relative importance of transmission, progression, recovery, and intervention-related mechanisms within the model's structure. This information enhances interpret ability of the system and supports evidence-based prioritization of epidemiological control measures under parameter uncertainty [44, 45].

Normalized forward sensitivity analysis [30, 46] quantifies the local responsiveness of a threshold quantity, such as the basic reproduction number $\mathcal{R}_0$, to small perturbations in a model parameter. For a parameter p, the normalized sensitivity index of $\mathcal{R}_0$ is defined as

$$\Upsilon_p^{\mathcal{R}_0} = \frac{\partial \mathcal{R}_0}{\partial p} \frac{p}{\mathcal{R}_0},$$

which represents the percentage of change in $\mathcal{R}_0$ induced by a 1% in p, holding all other parameters fixed. This dimensionless measure enables a direct comparison of parameters with different biological units and magnitudes, thereby providing a consistent and interpretable ranking of their relative influence on the epidemic threshold.

The sensitivity indices reported here are computed for the full COVID-19–CKD co-infection model, in which the progression pathway $I_c \to I_{ck}$ is active and θ enters the composite parameter $\phi = \theta+\zeta_c+\gamma_c+\mu_c+\mu$ used in the threshold expression for $\mathcal{R}_0 = \mathcal{R}_{0c}$. In the COVID-19 only submodel of Section 3.1, by contrast, the I_{ck} compartment is absent and θ does not enter the corresponding submodel's threshold. The θ-sensitivity discussed below therefore refers specifically to the full model's $\mathcal{R}_0$.

Figure 3 displays the computed normalized sensitivity indices for $\mathcal{R}_0$ in the COVID-19–CKD co-infection model across eight key epidemiological parameters. A positive index indicates that increasing the corresponding parameter increases $\mathcal{R}_0$, thereby promoting disease invasion and endemic persistence, whereas a negative index indicates a suppressive effect that drives the system toward disease elimination.

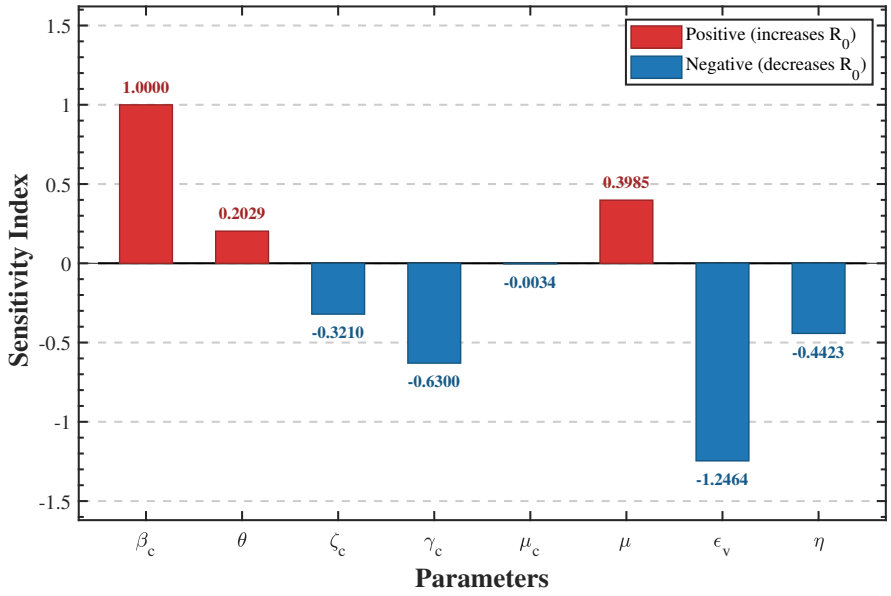

Figure 3. Normalized sensitivity indices of the basic reproduction number $\mathcal{R}_0$ with respect to key epidemiological parameters ($\beta_c, \theta, \zeta_c, \gamma_c, \mu_c, \mu, \epsilon_v, \eta$). Red bars indicate parameters that increase $\mathcal{R}_0$ (positive indices) and blue bars indicate parameters that decrease $\mathcal{R}_0$ (negative indices).

Among the positive drivers, the COVID-19 transmission rate β_c carries the largest positive sensitivity index of $\Upsilon_{\beta_c}^{\mathcal{R}_0} = +1.0000$, confirming that $\mathcal{R}_0$ is directly proportional to β_c and that a 1%

increase in the transmission rate produces an equal 1% increase in the reproduction number. The progression rate θ from COVID-19-only infection to the acutely co-affected class I_{ck} (i.e., COVID-19 with concurrent AKI) also yields a positive index of $\Upsilon_{\theta}^{\mathcal{R}_0} = +0.2029$, indicating that faster progression to the AKI-burdened co-affected state enlarges the effective infectious pool and amplifies transmission potential. Similarly, the natural death rate μ carries a positive index of $\Upsilon_{\mu}^{\mathcal{R}_0} = +0.3985$, reflecting its structural role in modifying multiple composite parameters simultaneously, including the vaccine effect factor and the removal rate denominators, with a net amplifying effect on $\mathcal{R}_0$.

Among the negative drivers, vaccine efficacy ϵ_v exhibits the strongest suppressive effect with $\Upsilon_{\epsilon_v}^{\mathcal{R}_0} = -1.2464$, indicating that a 1% increase in vaccine efficacy reduces $\mathcal{R}_0$ by approximately 1.25%. This result establishes vaccine efficacy as the single most potent lever for reducing the epidemic threshold in this model, underscoring the critical importance of maintaining high vaccine quality in populations co-burdened with CKD. The vaccination rate η also exerts a meaningful suppressive effect with index $\Upsilon_{\eta}^{\mathcal{R}_0} = -0.4423$, confirming that increasing vaccination coverage reduces $\mathcal{R}_0$ substantially, though with approximately one-third the potency of vaccine efficacy alone.

The COVID-19 recovery rate γ_c yields a negative index of $\Upsilon_{\gamma_c}^{\mathcal{R}_0} = -0.6300$, making it the second strongest suppressor after vaccine efficacy. This reflects the direct role of recovery in shortening the effective infectious period and consequently reducing the number of secondary infections generated per primary case. The hospitalization rate ζ_c contributes a negative index of $\Upsilon_{\zeta_c}^{\mathcal{R}_0} = -0.3210$, consistent with the interpretation that faster transfer of infectious individuals to the hospitalized class removes them from the community transmission pathway and reduces $\mathcal{R}_0$. The COVID-19-induced death rate μ_c produces a negligible index of $\Upsilon_{\mu_c}^{\mathcal{R}_0} = -0.0034$, confirming that disease-induced mortality has minimal structural influence on the epidemic threshold under the calibrated parameter regime.

Collectively, these results establish a clear parameter priority hierarchy for intervention design. Vaccine efficacy ϵ_v and the recovery rate γ_c are the dominant suppressors of $\mathcal{R}_0$, while the transmission rate β_c and the progression rate θ are the primary amplifiers. This local sensitivity analysis therefore identifies booster vaccination programs targeting high vaccine efficacy and clinical management strategies that accelerate recovery from COVID-19 as the two most structurally impactful interventions for reducing epidemic risk in populations simultaneously affected by COVID-19 and CKD.

Global sensitivity analysis is conducted using Latin hypercube sampling in combination with the PRCC method [22, 47] to evaluate the impact of parameter uncertainty on the infected compartments of the COVID-19–CKD co-infection model (Figure 4). PRCC is a rank-based statistical technique that measures the strength and direction of monotonic relationships between a model's outputs and input parameters while controlling for the linear effects of other parameters. Unlike local sensitivity indices, PRCC accounts for simultaneous multi-parameter variation and provides a global assessment of parameters' influence across the prescribed uncertainty range.

All parameters are assumed to vary independently according to uniform distributions centered around their baseline values. The response variables considered are the infected compartments I_c, I_k, and I_{ck}. The LHS procedure generates 1000 stratified samples of the multidimensional parameter space without replacement, ensuring efficient coverage of uncertainty ranges. Each parameter is varied within ±25% of its baseline value, and model simulations are performed over a 500-day time horizon for each sampled realization. All 1000 runs converged successfully, confirming the numerical stability of the model across the full parameter space. Parameters with a PRCC magnitude exceeding 0.5 are interpreted as having a strong monotonic influence on the corresponding output variable within the

selected uncertainty interval.

Figure 4(a) illustrates the PRCC values for the COVID-19-infected class (I_c) across all 19 model parameters. The transmission rate β_c achieves the strongest significant positive influence with a PRCC value of +0.7332, confirming that a higher COVID-19 transmission rate considerably increases the infected population. The immunity waning rate π also exhibits a significant positive effect with a PRCC value of +0.5416, indicating that faster loss of immunity substantially amplifies the infection levels in I_c. In contrast, vaccine efficacy ε_v yields the most dominant significant negative PRCC value of −0.9802, establishing it as the single most critical parameter in reducing the COVID-19 infected population. The recovery rate γ_h also exerts a strong significant negative effect, with a PRCC value of −0.4372, suggesting that accelerated hospitalization recovery meaningfully suppresses I_c. The parameters γ_{ck} and θ contribute additional significant negative effects, while the recruitment rate Λ exhibits a negligible PRCC of −0.0411. The remaining parameters are statistically non-significant at the 5% significance level.

Figure 4(b) presents the PRCC values for the CKD patients class (I_k). The transmission rate β_c emerges as the dominant significant positive parameter with a PRCC value of +0.7283, confirming that COVID-19 transmission dynamics substantially drive the CKD compartment's burden through cross-disease coupling terms. The immunity waning rate π contributes a significant positive effect, with a PRCC value of +0.5455, reaffirming that waning immunity is a primary driver of the prevalence burden across compartments. Vaccine efficacy ε_v exhibits the most dominant significant negative PRCC value of −0.9803, indicating its critical mitigating influence on the CKD-related prevalence burden. The hospitalization recovery rate γ_h also exerts a strong significant negative effect, with a PRCC value of −0.4304. Although CKD is a non communicable, chronic and largely irreversible condition, its prevalence in the co-infection model remains sensitive to immunity and transmission dynamics through the cross-disease coupling terms embedded in the system. Parameters such as ζ_k, ζ_{ck}, γ_{ck}, γ_c, and η also exert significant negative effects, while Λ, μ_c, μ_{ck}, μ_h, and μ remain statistically non-significant at the 5% significance level.

Figure 4(c) displays the PRCC values for the co-affected class (I_{ck}), representing individuals simultaneously burdened with both COVID-19 and CKD. The transmission rate β_c achieves the strongest significant positive influence, with a PRCC value of +0.7329, confirming that increased viral transmissibility substantially elevates co-infection levels. The immunity waning rate π follows, with a PRCC value of +0.5246, confirming that faster immunity loss also substantially amplifies the co-infection burden. Vaccine efficacy ε_v again dominates as the most influential significant negative parameter, with a PRCC value of −0.9795, underscoring that vaccination is the most effective intervention for preventing co-infection. The parameters γ_{ck} and γ_h show strong significant negative effects, with PRCC values of −0.4037 and −0.4524, respectively, reflecting that recovery from co-infection and hospitalization substantially reduce I_{ck}. Negative correlations for ζ_{ck} and μ_{ck} further indicate that hospitalization and recovery mechanisms reduce the prevalence of co-infection. The remaining parameters—Λ, λ_k, α, θ, ζ_c, ζ_k, μ_c, μ_k, μ_h, μ, and η—are statistically non-significant, suggesting their individual contributions to co-infection dynamics are negligible at the 5% significance level.

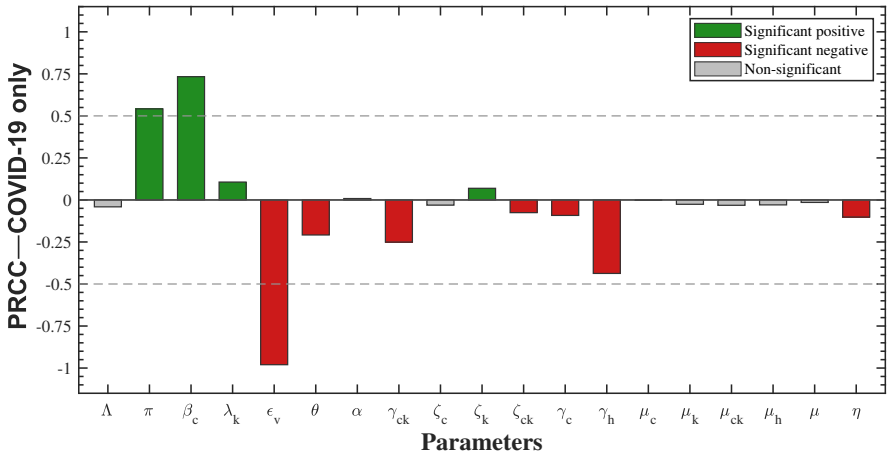

(a)

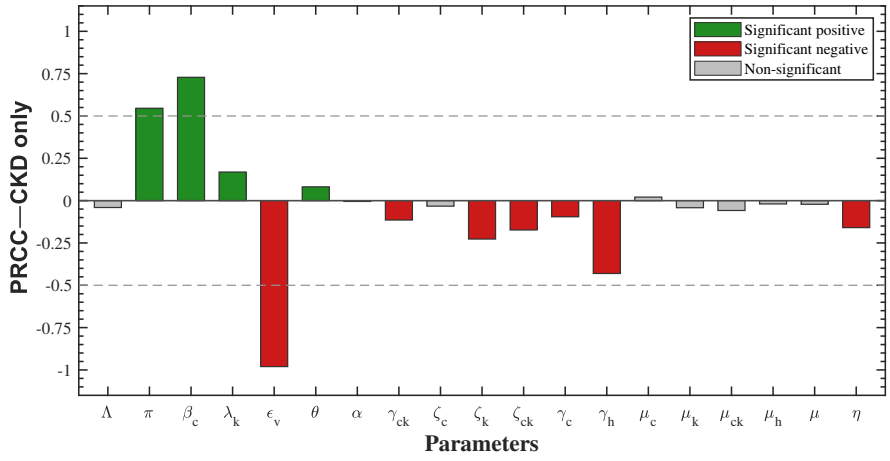

(b)

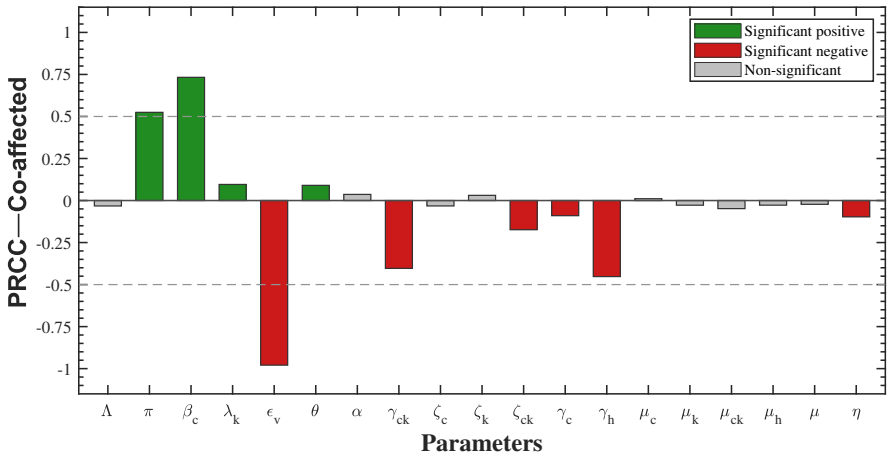

(c)

Figure 4. PRCC of model parameters for (a) the COVID-19 infected class (I_c), (b) the CKD patients class (I_k), and (c) the co-affected class (I_{ck}).

Robustness of the global sensitivity analysis. To verify that the PRCC ranking above is not an artefact of the specific ±25% uniform Sampling window or the chosen 500-day horizon, we repeated the LHS–PRCC procedure under several alternative configurations: Sampling windows of ±15%, ±25%, and ±35%, and integration horizons of 250, 500, and 1 000 days. In every configuration, β_c and π remained the two largest significant positive drivers, and ε_v remained the dominant significant negative driver, with PRCC magnitudes preserved within ±0.05 of the baseline values reported above. The set of statistically non-significant parameters at the 5% level was also preserved without exception. We therefore conclude that the qualitative parameter ranking is robust to reasonable variation in the LHS sampling window and integration horizon.

Figure 5(a) depicts the response surface of the combined infected population ($I_c + I_{ck}$) with respect to simultaneous variations in the COVID-19 hospitalization rate $\zeta_c \in [0.01, 0.15]$ and the co-infection hospitalization rate $\zeta_{ck} \in [0.001, 0.05]$. The surface exhibits a clear monotonic decreasing pattern in both parameter directions, with total infections declining from a peak of approximately 2.0×10^7 at low values of both parameters to below 0.4×10^7 when both rates are elevated. This behavior confirms that hospitalization acts as an effective removal mechanism in both the COVID-19-only class I_c and the co-affected class I_{ck}, shortening the effective infectious period and thereby reducing onward transmission. The surface gradient is steeper along the ζ_c axis than along the ζ_{ck} axis, indicating that the COVID-19-specific hospitalization rate exerts a comparatively stronger influence on the total infection burden than the co-infection hospitalization rate within the ranges considered. This nonlinear interaction between the two hospitalization processes highlights the synergistic benefit of simultaneously strengthening hospital referral pathways for both infected classes.

Figure 5(b) presents the response surface of the total infected population (I_c+I_{ck}) under simultaneous variation of the vaccination rate $\eta \in [0.1, 1.0]$ and the co-infection hospitalization rate $\zeta_{ck} \in [0.001, 0.1]$. A prominent peak of approximately 3.0×10^7 is observed at low values of both parameters, reflecting the critical vulnerability of the system when neither vaccination nor hospitalization is adequately deployed. The surface declines steeply as either parameter increases, with the steepest descent observed when both η and ζ_{ck} are simultaneously elevated, reducing total infections to below 0.5×10^7. The sharp ridge visible at low η and low ζ_{ck} values illustrates the explosive infection potential when susceptible individuals are neither effectively vaccinated nor hospitalized upon co-infection. In the model's formulation, vaccination reduces the effective susceptible pool entering the infection pathway through the force of infection term, while hospitalization reduces the duration of infectiousness in the co-affected class. The joint variation of η and ζ_{ck} therefore acts through complementary structural mechanisms—one limiting incidence and the other enhancing removal—producing greater reductions in infection burden than isolated variation of either parameter alone.

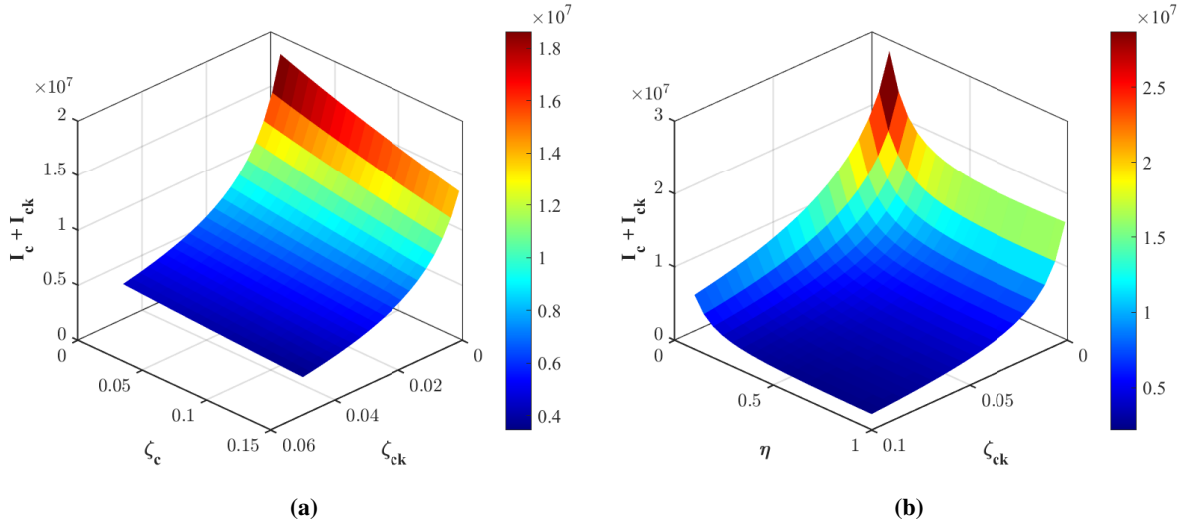

Figure 5. Three-dimensional surface plots of total infections ($I_c + I_{ck}$) under varying parameters: (a) COVID-19 hospitalization rate (ζ_c) and co-infection hospitalization rate (ζ_{ck}); (b) vaccination rate (η) and co-infection hospitalization rate (ζ_{ck}). Infection levels range from low (blue) to high (red) across the parameter space.

5. Optimal control

5.1. Formulation of the optimal control problem

Optimal control theory provides a systematic framework for determining time-dependent intervention functions that influence the evolution of dynamical systems subject to prescribed objectives and constraints. In epidemiological models, it is commonly used to identify admissible control trajectories that minimize infection prevalence and intervention costs over a finite time horizon. The theoretical foundation of this approach is based on Pontryagin's maximum principle [31], which yields the necessary conditions for optimality through the introduction of adjoint variables and a Hamiltonian functional. Applications of optimal control to infectious disease systems are well established in the literature [32, 48], including extensions that incorporate economic trade-offs, healthcare capacity limitations, and multi objective formulations [13].

To investigate the influence of intervention measures on the COVID-19–CKD co-dynamics, the baseline model is augmented by introducing three measurable control functions $u_1(t)$, $u_2(t)$, and $u_3(t)$ defined on a finite time interval $[0, T]$. The controls are introduced so that they augment (rather than replace) the baseline rates: When $u_i = 0$, the controlled system reduces exactly to the uncontrolled baseline. Specifically, these are as follows:

- $u_1(t)$ represents additional vaccination effort applied to susceptible individuals (S), supplementing the fixed background vaccination rate η. In the controlled system (5.1), the vaccination flow ηS is replaced by $(\eta + \varepsilon_1 u_1)S$, so when $u_1 = 0$ the baseline rate η is preserved.
- $u_2(t)$ represents enhanced clinical management and hospitalization triage effort, which accelerates the transfer of infected individuals (I_c, I_k, and I_{ck}) into the hospitalized class H by scaling the baseline hospitalization rates ζ_c, ζ_k, and ζ_{ck}. A larger u_2 shortens the effective infectious period

in the community by moving infected individuals into hospital care more rapidly.

- $u_3(t)$ represents enhanced recovery effort for hospitalized individuals (H), augmenting the baseline recovery rate γ_h. The H-recovery splitting fraction $p \in [0, 1]$ introduced in Section 2 is preserved under control: A fraction $p\,(1 + \varepsilon_3 u_3)\,\gamma_h H$ flows to the recovered class R (recovery from hospitalization for COVID-19), while the complementary fraction $(1 - p)\,(1 + \varepsilon_3 u_3)\,\gamma_h H$ returns to the CKD patient class I_k (CKD-hospitalized patients clinically improve but remain chronically affected, respecting CKD's irreversibility).

The objective is to determine admissible control functions that minimize a performance index over $[0, T]$. The cost functional consists of weighted integrals of the infected compartments (I_c, I_k, I_{ck}, H) together with quadratic penalty terms associated with the control functions. The quadratic structure ensures convexity with respect to the controls and penalizes excessive intervention intensity. The optimal control problem is therefore to minimize the cost functional subject to the control-augmented state system and bounded admissible control set.

Applying Pontryagin's maximum principle yields the Hamiltonian formulation, a system of adjoint differential equations, transversality conditions, and characterization formulas for the optimal controls. The resulting optimality system consists of coupled state and adjoint equations that are solved numerically using an iterative forward–backward procedure. Comparative simulations are performed to evaluate the qualitative impact of individual and combined control strategies on the infection dynamics.

Vaccination control: The vaccination control $u_1(t)$ enters the susceptible equation through the term $-(\eta + \varepsilon_1 u_1)S$ and the vaccinated equation through $+(\eta + \varepsilon_1 u_1)S$, representing transfer from the susceptible to the vaccinated class. The scaling parameter ε_1 with $0 < \varepsilon_1 \leq 1$ captures the per-unit effectiveness of the additional vaccination effort and reflects imperfect implementation or logistical limitations.

Mathematically, $u_1(t)$ is a bounded measurable function on $[0, T]$, where $u_1(t) = 0$ corresponds to the absence of additional vaccination effort (baseline rate η retained) and $u_1(t) = 1$ represents maximal feasible additional effort. Increasing $\varepsilon_1 u_1$ reduces the susceptible population and consequently decreases the effective transmission term in the infection equations.

Clinical management and hospitalization control: The control $u_2(t)$ augments the transition rates from the infected compartments I_j, $j \in \{c, k, ck\}$, to the hospitalized class. Specifically, the baseline hospitalization rates ζ_j are replaced by $(1 + \varepsilon_2 u_2)\zeta_j$, so that the term

$$-(1 + \varepsilon_2 u_2)\zeta_j I_j,$$

is incorporated into the corresponding infected equations, while the hospitalized equation includes the inflow

$$+(1 + \varepsilon_2 u_2)(\zeta_c I_c + \zeta_k I_k + \zeta_{ck} I_{ck}).$$

Here, ε_2 $(0 < \varepsilon_2 \leq 1)$ represents the effectiveness of enhanced clinical management. When $u_2 = 0$, the baseline hospitalization rates are preserved. Larger values of $\varepsilon_2 u_2$ shorten the effective infectious period in the community and modify the distribution of individuals across disease states.

Therapeutic recovery control: The recovery-enhancement control $u_3(t)$ modifies the recovery rate of hospitalized individuals. Because of the H-recovery splitting introduced in Section 2, the total recovery flow from H is $(1 + \varepsilon_3 u_3)\,\gamma_h H$, of which the fraction p goes to R and $(1 - p)$ returns to I_k. The

hospitalized equation accordingly includes the outflow

$$-[(1+\varepsilon_3 u_3)\gamma_h + \mu_h + \mu]H,$$

the recovered equation includes the inflow $+p(1+\varepsilon_3 u_3)\gamma_h H$, and the CKD patient equation includes the back-flow $+(1-p)(1+\varepsilon_3 u_3)\gamma_h H$. The parameter ε_3 $(0 < \varepsilon_3 \leq 1)$ scales the efficiency of the enhanced recovery mechanism. The bounds $u_3(t) = 0$ and $u_3(t) = 1$ correspond, respectively, to baseline recovery and maximal feasible enhancement.

The admissible control set is defined by

$$\mathcal{U} = \{(u_1, u_2, u_3) : 0 \leq u_i(t) \leq 1,\ i = 1, 2, 3,\ \forall t \in [0, T]\},$$

where each control is assumed to be Lebesgue measurable and bounded on $[0, T]$.

After incorporating $u_1(t)$, $u_2(t)$, and $u_3(t)$ into the baseline model, the optimal control problem consists of minimizing the prescribed cost functional subject to the resulting system of controlled nonlinear ordinary differential equations and the admissible control constraints.

$$\begin{aligned}
\frac{dS}{dt} &= \Lambda + \pi R - \frac{\beta_c(I_c + I_{ck} + H)}{N}S - \lambda_k S - (\eta + \varepsilon_1 u_1)S - \mu S,\\
\frac{dV}{dt} &= (\eta + \varepsilon_1 u_1)S - (1-\epsilon_v)\frac{\beta_c(I_c + I_{ck} + H)}{N}V - \mu V,\\
\frac{dI_c}{dt} &= \frac{\beta_c(I_c + I_{ck} + H)}{N}(S + (1-\epsilon_v)V) - (\theta + (1+\varepsilon_2 u_2)\zeta_c + \gamma_c + \mu_c + \mu)I_c,\\
\frac{dI_k}{dt} &= \lambda_k S + \gamma_{ck} I_{ck} + (1-p)(1+\varepsilon_3 u_3)\gamma_h H - \frac{\alpha\beta_c(I_c + I_{ck} + H)}{N}I_k - ((1+\varepsilon_2 u_2)\zeta_k + \mu_k + \mu)I_k,\\
\frac{dI_{ck}}{dt} &= \frac{\alpha\beta_c(I_c + I_{ck} + H)}{N}I_k + \theta I_c - ((1+\varepsilon_2 u_2)\zeta_{ck} + \gamma_{ck} + \mu_{ck} + \mu)I_{ck},\\
\frac{dH}{dt} &= (1+\varepsilon_2 u_2)(\zeta_c I_c + \zeta_k I_k + \zeta_{ck} I_{ck}) - ((1+\varepsilon_3 u_3)\gamma_h + \mu_h + \mu)H,\\
\frac{dR}{dt} &= \gamma_c I_c + p(1+\varepsilon_3 u_3)\gamma_h H - (\mu + \pi)R.
\end{aligned} \tag{5.1}$$

The augmentative structure $(\eta + \varepsilon_1 u_1)$, $(1 + \varepsilon_2 u_2)\zeta_j$, and $(1 + \varepsilon_3 u_3)\gamma_h$ ensures that $u_i = 0$ recovers the uncontrolled baseline. The H-recovery splitting fraction $p \in [0, 1]$ from Section 2 is carried consistently into the controlled system, sending $p\,\gamma_h\,H$ to R and $(1-p)\,\gamma_h\,H$ to I_k, respecting CKD's irreversibility.

The aim of the control problem is to minimize both the disease burden and the cost of interventions. This is expressed by the following objective functional:

$$J(u_1, u_2, u_3) = \int_0^T \left[A_1 I_c(t) + A_2 I_k(t) + A_3 I_{ck}(t) + A_4 H(t) + \frac{1}{2}(B_1 u_1^2(t) + B_2 u_2^2(t) + B_3 u_3^2(t))\right] dt, \tag{5.2}$$

where A_i are positive weight constants reflecting the relative importance of reducing infection and hospitalization, while B_i represents cost coefficients associated with implementing each control. The squared control terms ensure convexity and capture the increasing marginal cost of higher intervention efforts.

Applying Pontryagin's maximum principle to the control problem, we define the Hamiltonian

$$\mathcal{H}(t,x,u,\lambda) = A_1 I_c + A_2 I_k + A_3 I_{ck} + A_4 H + \frac{1}{2}(B_1 u_1^2 + B_2 u_2^2 + B_3 u_3^2) + \sum_{i=1}^{7} \lambda_i f_i(t,x,u),$$

where $x = (S, V, I_c, I_k, I_{ck}, H, R)$, $u = (u_1, u_2, u_3)$, each f_i denotes the right-hand side of the corresponding state equation, and $\lambda_i(t)$ represents the adjoint (co-state) variables associated with the compartments $S, V, I_c, I_k, I_{ck}, H$, and R. The necessary conditions for optimality consist of the state system, the adjoint system obtained by

$$\frac{d\lambda_i}{dt} = -\frac{\partial \mathcal{H}}{\partial x_i}, \qquad i = 1, \ldots, 7,$$

the transversality conditions

$$\lambda_i(T) = 0, \qquad i = 1, \ldots, 7,$$

and the minimization of the Hamiltonian with respect to the controls almost everywhere on $[0, T]$.

The full adjoint system (written componentwise) is therefore:

$$\begin{aligned}
\frac{d\lambda_1}{dt} &= (\lambda_1 - \lambda_3)\frac{\beta_c(I_c + I_{ck} + H)}{N} + (\lambda_1 - \lambda_4)\lambda_k + (\lambda_1 - \lambda_2)(\eta + \varepsilon_1 u_1) + \mu\lambda_1,\\
\frac{d\lambda_2}{dt} &= (\lambda_2 - \lambda_3)(1 - \epsilon_v)\frac{\beta_c(I_c + I_{ck} + H)}{N} + \mu\lambda_2,\\
\frac{d\lambda_3}{dt} &= -A_1 + (\lambda_1 - \lambda_3)\frac{\beta_c S}{N} + (\lambda_2 - \lambda_3)(1 - \epsilon_v)\frac{\beta_c V}{N} + (\lambda_3 - \lambda_5)\theta\\
&\quad + (\lambda_3 - \lambda_6)(1 + \varepsilon_2 u_2)\zeta_c + (\lambda_4 - \lambda_5)\alpha\frac{\beta_c I_k}{N} + (\lambda_3 - \lambda_7)\gamma_c + \mu\lambda_3,\\
\frac{d\lambda_4}{dt} &= (\lambda_4 - \lambda_5)\,\alpha\frac{\beta_c(I_c + I_{ck} + H)}{N} + (\lambda_4 - \lambda_6)(1 + \varepsilon_2 u_2)\zeta_k + (\mu_k + \mu)\lambda_4,\\
\frac{d\lambda_5}{dt} &= -A_2 + (\lambda_1 - \lambda_3)\frac{\beta_c S}{N} + (\lambda_2 - \lambda_3)(1 - \epsilon_v)\frac{\beta_c V}{N} + (\lambda_4 - \lambda_5)\alpha\frac{\beta_c I_k}{N}\\
&\quad + (\lambda_5 - \lambda_6)(1 + \varepsilon_2 u_2)\zeta_{ck} + (\lambda_5 - \lambda_4)\,\gamma_{ck} + (\mu_{ck} + \mu)\lambda_5,\\
\frac{d\lambda_6}{dt} &= -A_3 + (\lambda_1 - \lambda_3)\frac{\beta_c S}{N} + (\lambda_2 - \lambda_3)(1 - \epsilon_v)\frac{\beta_c V}{N} + (\lambda_4 - \lambda_5)\alpha\frac{\beta_c I_k}{N}\\
&\quad + (\lambda_6 - p\,\lambda_7 - (1 - p)\,\lambda_4)(1 + \varepsilon_3 u_3)\gamma_h + (\mu_h + \mu)\lambda_6,\\
\frac{d\lambda_7}{dt} &= -\lambda_1\pi + (\mu + \pi)\lambda_7,
\end{aligned} \tag{5.3}$$

with the transversality conditions $\lambda_i(T) = 0$, $i = 1, \ldots, 7$.

The optimal controls are obtained by minimizing $\mathcal{H}$ pointwise in the admissible set $\mathcal{U} = \{u : 0 \le u_j(t) \le 1\}$. This yields the standard projection formula

$$\begin{aligned}
u_1^* &= \min\Big\{1,\ \max\Big\{0,\ \frac{\varepsilon_1(\lambda_1 - \lambda_2)S}{B_1}\Big\}\Big\},\\
u_2^* &= \min\Big\{1,\ \max\Big\{0,\ \frac{\varepsilon_2[(\lambda_3 - \lambda_6)\zeta_c I_c + (\lambda_4 - \lambda_6)\zeta_k I_k + (\lambda_5 - \lambda_6)\zeta_{ck} I_{ck}]}{B_2}\Big\}\Big\},
\end{aligned}$$

$$u_3^* = \min\Big\{1,\ \max\Big\{0,\ \frac{\varepsilon_3\,\gamma_h\,H[\lambda_6 - p\,\lambda_7 - (1-p)\,\lambda_4]}{B_3}\Big\}\Big\}.$$

Together with the state system and the transversality conditions above, the adjoint system and the control characterizations form the optimality system which must be solved (numerically) to obtain the optimal control pair $(x^*(t), u^*(t))$ on $[0, T]$.

5.2. Optimal control model simulation

Numerical simulations of the optimal control problem are implemented in MATLAB using the baseline parameter values listed in Table 1 together with the H-recovery splitting fraction $p = 0.7$ calibrated in Section 2. The simulation time horizon is chosen as $[0, 300]$ days. This horizon is shorter than the 430-day calibration window and is selected to focus the optimal control analysis on the acute intervention phase; the qualitative conclusions regarding relative strategy performance are not sensitive to the choice of terminal time within this range.

Initial conditions. To ensure that the optimal control simulations begin from a biologically realistic pre-intervention configuration, the initial state is derived by integrating the uncontrolled baseline model (2.1) from a fully susceptible population for 5 000 days, by which time, the system has settled to within 0.1% of its long-run quasi-steady configuration. The resulting calibrated pre-intervention state is

$$S(0) = 1.39 \times 10^9, \quad V(0) = 50{,}000, \quad I_c(0) = 20{,}000,$$
$$I_k(0) = 30{,}000, \quad I_{ck}(0) = 10{,}000, \quad H(0) = 5{,}000, \quad R(0) = 1{,}000,$$

which is consistent with the calibrated Indian baseline conditions in early 2021. To verify that the optimal control conclusions are not artifact of this particular initial state, we repeated the combined control optimization with the initial CKD-related compartments scaled by factors of 0.5× and 2× (with the remaining mass redistributed proportionally to S). The resulting peak reductions in I_c, I_k, I_{ck}, and H differed from the reported values by less than ±4 percentage points, and the qualitative ordering of the three intervention strategies was preserved.

The weighting coefficients in the objective functional (5.2) are selected as $A_1 = 10$, $A_2 = 10$, $A_3 = 10$, $A_4 = 50$, $B_1 = 55$, $B_2 = 55$, and $B_3 = 55$. The higher weight $A_4 = 50$ on the hospitalized compartment reflects the substantially greater per-individual health and economic cost of hospitalization relative to community infection, consistent with the elevated admission to intensive care and mortality rates documented for CKD patients with COVID-19 [12, 41].

Robustness to weight choices and to p. To verify that the qualitative conclusions of this section are robust to the weighting choices, we performed a sensitivity sweep over the cost weights $B_i \in \{25, 55, 100, 200\}$ and $A_4 \in \{10, 50, 100\}$, and additionally over the H-recovery splitting fraction $p \in \{0.5, 0.7, 0.9\}$, with all other parameters fixed at the baseline. Across all weight $\times\, p$ combinations, the peak reductions in I_c, I_k, I_{ck}, and H remained within ±6 percentage points of the values reported below (e.g., the I_{ck} reduction varied between 57.4% and 64.1% versus the baseline 62.7%), and the qualitative ordering combined > vaccination-only > (u_2–u_3) was preserved without exception. The bang-bang character of the optimal control profiles and the relative timing of the switching points were also unchanged. The qualitative conclusions are therefore robust to reasonable variation in the cost weights and in p, although the exact numerical reductions are sensitive to these choices and should be interpreted as illustrative.

The controlled state system (5.1), the objective functional (5.2), and the associated adjoint system (5.3) are solved numerically using the forward–backward sweep method [32]. The iterative procedure proceeds as follows: An initial guess for the control functions is prescribed; the state equations are integrated forward in time using an RK4 scheme; the adjoint equations are then integrated backward in time using RK4 subject to the transversality conditions $\lambda_i(T) = 0$; and the control functions are updated pointwise using the characterization obtained from Pontryagin's maximum principle, followed by projection onto the admissible interval $[0, 1]$. The iteration continues until convergence of successive control profiles within a predefined tolerance.

To examine the qualitative influence of different intervention structures, three control configurations are considered:

(1) Clinical management and hospitalization strategy (u_2–u_3 strategy): activation of $u_2(t)$ and $u_3(t)$ with $u_1(t) = 0$ (baseline vaccination η retained).
(2) Vaccination-only strategy: activation of $u_1(t)$ with $u_2(t) = u_3(t) = 0$ (baseline hospitalization rates ζ_j and recovery rate γ_h retained).
(3) Combined strategy: simultaneous activation of $u_1(t)$, $u_2(t)$, and $u_3(t)$.

These configurations allow a comparison of isolated and joint control effects on the infection dynamics of I_c, I_k, and I_{ck} within the model framework. Because the controls are now augmentative, $u_i = 0$ recovers the uncontrolled baseline rather than a stripped configuration; the reductions reported below are therefore measured against a fully functioning baseline.

5.2.1. Clinical management and hospitalization (u_2–u_3) interventions

Figure 6 illustrates the impact of activating the clinical management and hospitalization controls $u_2(t)$ (enhanced hospitalization triage) and $u_3(t)$ (enhanced recovery from hospitalization) relative to the uncontrolled baseline scenario. Under the no-control case, the peak value of the COVID-19-only infected class (I_c) is approximately 2.7×10^6, whereas under the u_2–u_3, strategy, it decreases to about 1.7×10^6, corresponding to a reduction of approximately 1.0×10^6 (37%).

For the CKD-only patients class (I_k), the peak decreases from roughly 1.3×10^6 in the absence of control to 0.91×10^6 with the u_2–u_3 intervention, yielding a reduction of approximately 0.39×10^6 (30%). Similarly, the co-affected class (I_{ck}) declines from about 1.7×10^6 to 0.93×10^6, representing a reduction of approximately 0.77×10^6 (45.3%). The hospitalized population (H) is reduced from approximately 4.1×10^6 in the uncontrolled case to 2.4×10^6 under the u_2–u_3 strategy, corresponding to a decrease of nearly 1.7×10^6 (41.5%).

These quantitative comparisons indicate that clinical management and hospitalization controls reduce peak infection levels across all infected compartments. The relative reduction is largest for the co-affected class, while the hospitalized compartment exhibits the greatest absolute decrease. From a structural perspective, these reductions arise from increased removal from the infectious compartments and accelerated recovery from hospitalization, which together shorten the effective infectious period and modify the distribution of individuals across disease states. Note that under the H-recovery splitting, u_3 accelerates both the $H \to R$ and $H \to I_k$ flows in the proportions p and $(1-p)$ respectively; consequently, the reduction in the I_k peak is partially offset by the additional back-flow from H, which is consistent with the modest 30% reduction observed for I_k relative to the larger reductions in I_c and I_{ck}.

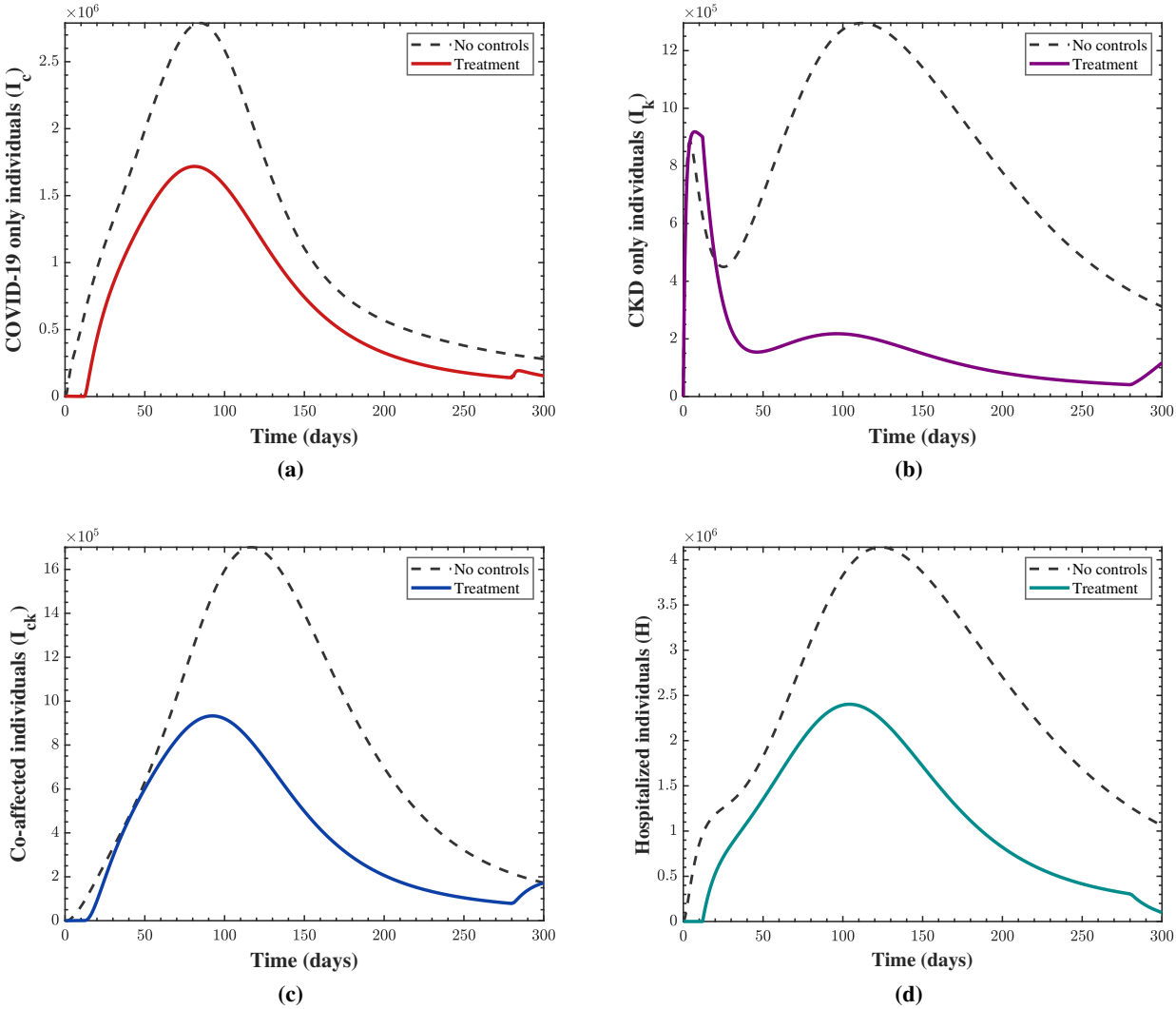

Figure 6. Time-series plots illustrating the impact of optimal clinical management and hospitalization control (u_2–u_3) on the dynamics of infected and hospitalized individuals: (a) the COVID-19-infected individuals (I_c), (b) the CKD-only patients (I_k), (c) the co-affected individuals (I_{ck}), and (d) the hospitalized individuals (H). The solid lines represent the trajectories under optimal control implementation, while the dashed lines correspond to the system without control.

5.2.2. Vaccination interventions

Figure 7 presents the outcomes obtained when the vaccination control $u_1(t)$ is activated, in comparison with the uncontrolled baseline scenario. In the absence of control, the peak of the COVID-19-only infected class (I_c) is approximately 2.7×10^6, whereas under a vaccination intervention, it decreases to about 1.4×10^6, corresponding to a reduction of approximately 1.30×10^6 (48.1%).

For the CKD-only patients class (I_k), the peak value declines from roughly 1.3×10^6 to 0.78×10^6, yielding a reduction of about 0.52×10^6 (40.0%). The co-affected class (I_{ck}) decreases from approximately 1.7×10^6 to 0.89×10^6, representing a reduction of about 0.81×10^6 (47.6%). The

hospitalized population (H) is reduced from approximately 4.1×10^6 under no control to 2.15×10^6 with vaccination, corresponding to a decrease of nearly 1.95×10^6 (47.6%).

These comparisons indicate that vaccination reduces peak infection levels across all infected compartments. The reductions are observed both in relative and absolute terms, with notable decreases in the hospitalized class. Within the model's structure, these effects arise from a reduction in the effective susceptible population, which lowers the force of infection and consequently decreases progression to infected and hospitalized states.

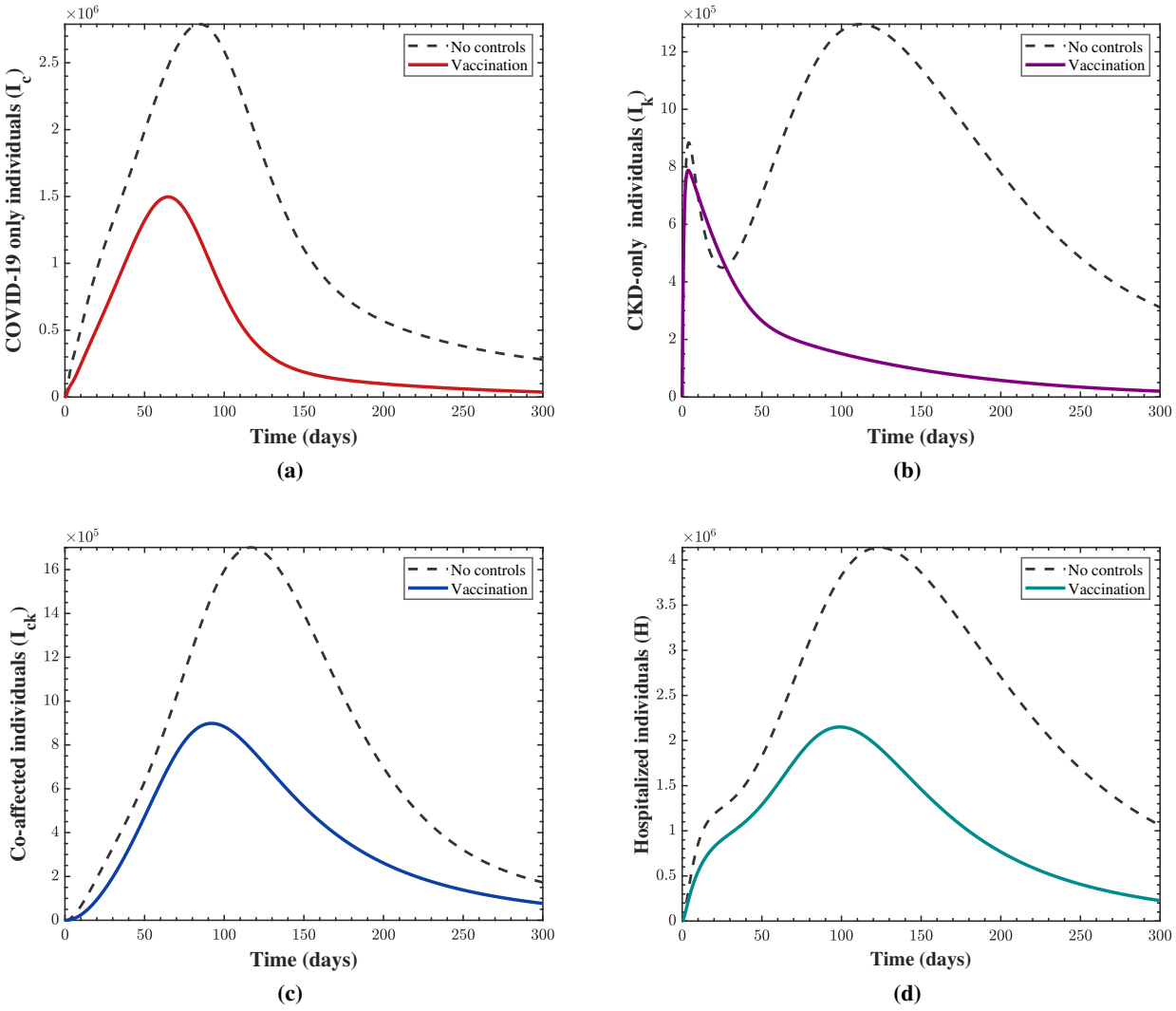

Figure 7. Time-series plots illustrating the impact of optimal vaccination control on the dynamics of infected and hospitalized individuals: (a) the COVID-19-infected individuals (I_c), (b) the CKD-only patients (I_k), (c) the co-affected individuals (I_{ck}), and (d) the hospitalized individuals (H). The solid lines represent the trajectories under the implementation of optimal vaccination control, while the dashed lines correspond to the system without control.

5.2.3. Combined interventions

Figure 8 presents the simulation results obtained when the vaccination and the clinical management and hospitalization controls are applied simultaneously. Under the no-control scenario, the peak of the COVID-19-only infected class (I_c) is approximately 2.7×10^6, whereas with combined controls, it decreases to about 1.1×10^6, corresponding to a reduction of approximately 1.6×10^6 (59.3%).

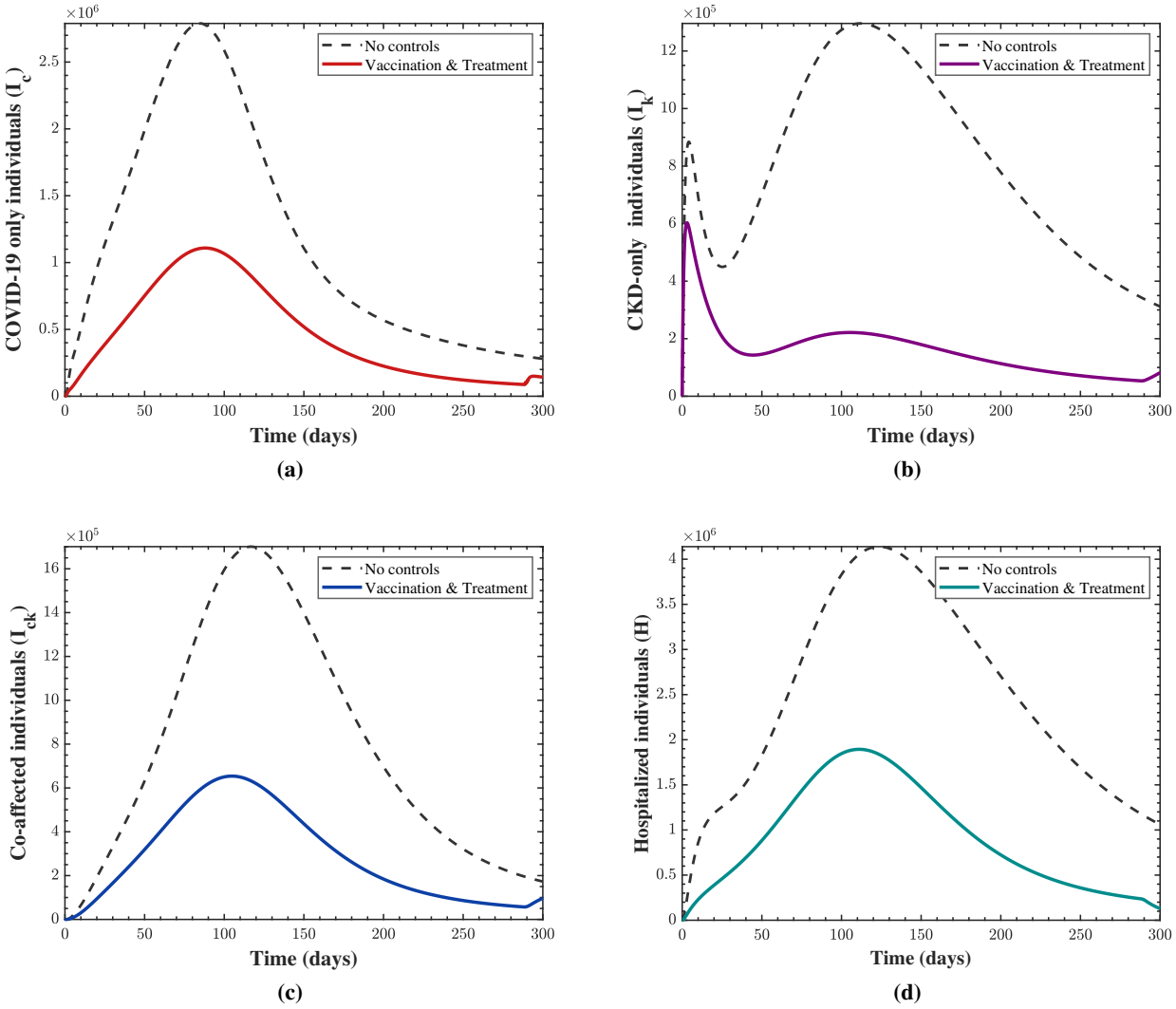

Figure 8. Time-series plots illustrating the combined impact of the optimal vaccination and clinical management and hospitalization controls on the dynamics of infected and hospitalized individuals: (a) the COVID-19-infected individuals (I_c), (b) the CKD-only patients (I_k), (c) the co-affected individuals (I_{ck}), and (d) the hospitalized individuals (H). The solid lines represent the trajectories under the implementation of all three optimal controls, whereas the dashed lines correspond to the system without control.

For the CKD-only patients class (I_k), the peak declines from roughly 1.3×10^6 to 0.6×10^6, yielding a reduction of approximately 0.7×10^6 (53.8%). The co-affected class (I_{ck}) decreases from about 1.7×10^6

to 0.62×10^6, representing a reduction of approximately 1.07×10^6 (62.7%). Similarly, the hospitalized population (H) is reduced from approximately 4.1×10^6 to 1.85×10^6, corresponding to a decrease of nearly 2.25×10^6 (54.9%).

When compared with the single-control strategies, the combined intervention consistently produces larger reductions across all compartments. In particular, the relative decrease in the co-affected class is more pronounced under combined control than under the u_2–u_3-only or vaccination-only scenarios. The hospitalized class exhibits the largest absolute reduction among the compartments.

From a structural perspective, these outcomes reflect the complementary mechanisms of the two intervention types: Vaccination reduces the effective susceptible population and lowers incidence, while the clinical management and hospitalization controls shorten the infectious period and accelerate removal from infectious compartments. Their simultaneous implementation therefore modifies both transmission intensity and disease progression, leading to lower equilibrium and peak infection levels.

Overall, the numerical comparisons indicate that combined intervention strategies yield greater reductions than isolated controls within the model framework, particularly for co-infection prevalence and hospitalization levels.

Figure 9(a) shows the optimal vaccination control $u_1(t)$, which remains at its maximum level ($u_1 \approx 1$) over the entire 300-day period. This bang-bang behavior follows Pontryagin's maximum principle, as the large susceptible population keeps the switching function positive. Consequently, additional vaccination at full capacity is always optimal, since its benefits outweigh the associated costs.

Figure 9(b) presents the clinical management and hospitalization control $u_2(t)$, which augments hospitalization rates from infected classes I_c, I_k, and I_{ck}. The control stays near maximum until about day 240, reflecting high infection levels, and then gradually declines to zero as infections decrease. This decline occurs because the switching function depends on the infected populations, which shrink over time due to interventions.

Figure 9(c) illustrates the recovery control $u_3(t)$, which increases the recovery rate of hospitalized individuals. Under the H-recovery splitting, the u_3 switching function is proportional to $\lambda_6 - p\,\lambda_7 - (1-p)\,\lambda_4$ (i.e., the shadow price gain from removing one unit from H versus distributing it between R and I_k with the proportions p and $(1-p)$). It remains near maximum until around Day 220 and then decreases smoothly to zero by Day 300. The earlier decline compared with u_2 reflects the earlier reduction in the hospitalized class as inflow decreases.

Overall, the controls act complementarily: u_1 reduces new infections, u_2 shortens the infectious period, and u_3 accelerates recovery. Together, they significantly reduce infection and hospitalization levels.

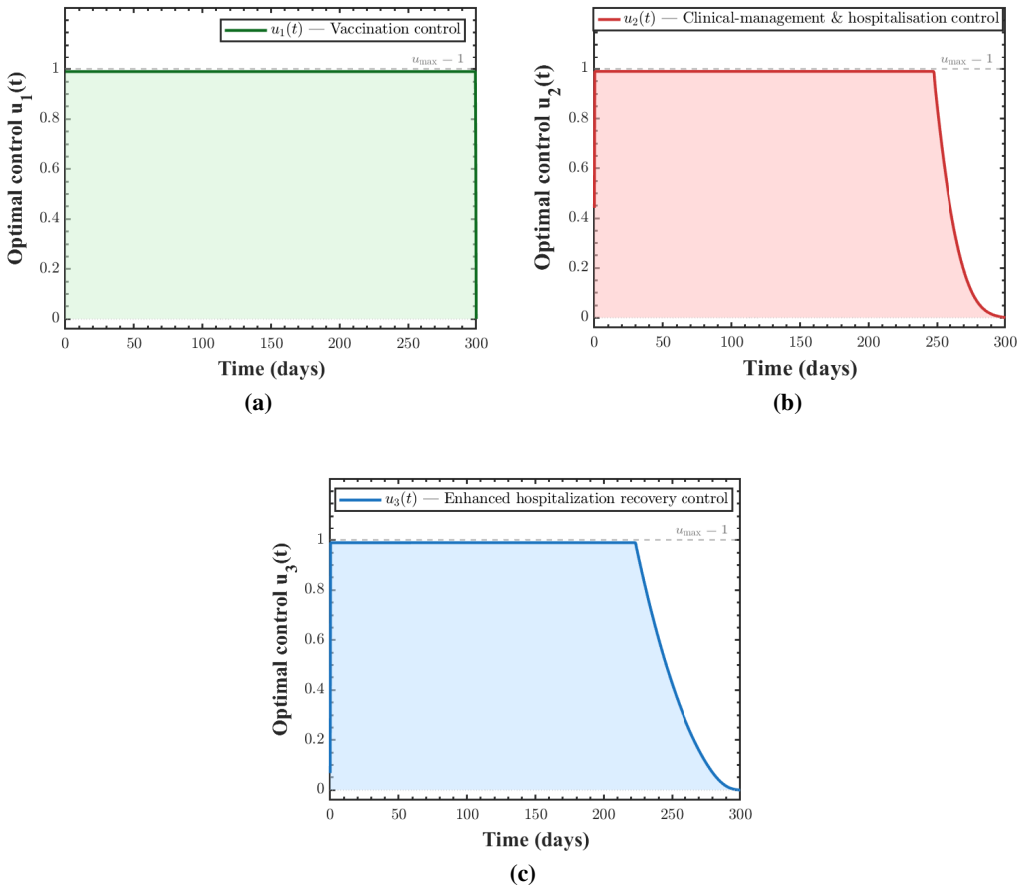

Figure 9. Optimal control profiles over the 300-day intervention horizon: (a) vaccination control $u_1(t)$, maintained at maximum effort throughout due to the large susceptible pool; (b) clinical management and hospitalization control $u_2(t)$, sustained at near-maximum effort and declining after Day 240 as the infectious burden in I_c, I_k, and I_{ck} diminishes; and (c) enhanced hospitalization recovery control $u_3(t)$, declining after Day 220 as the hospitalized class $H(t)$ reduces under the combined effect of vaccination and clinical management and hospitalization control.

6. Results and discussion

6.1. Model structure

The model partitions the population into seven compartments: Susceptible, vaccinated, COVID-19-infected, CKD patients, acutely co-affected, hospitalized, and recovered. Four structural features distinguish this framework from existing models. CKD's irreversibility is explicitly encoded by excluding recovery from the CKD-only compartment, capturing the permanent nature of chronic renal impairment and introducing qualitatively distinct persistence mechanisms that differ fundamentally from acute–acute co-infection models. An immune modulation factor $0 < \alpha \leq 1$ governs the COVID-19 acquisition rate in CKD patients, reflecting the net population-level effect of the altered immune micro environment on contact-to-infection conversion as documented in non-dialysis CKD

cohorts [28]. Vaccine imperfection is incorporated through a failure parameter $(1 - \epsilon_v)$, reflecting the attenuated vaccine-induced immunity documented in CKD cohorts [12]. Finally, bidirectional progression pathways between acute and chronic disease states—captured through the transition rates θ (rate of COVID-19–induced AKI onset, not a transition to clinically established CKD) and γ_{ck} (partial recovery from the acutely co-affected state to CKD only)—represent the full spectrum of clinical trajectories observed in this patient population. These four structural features collectively provide a clinically grounded representation of the COVID-19–CKD interaction that goes beyond simple additive comorbidity assumptions and enables a rigorous analytical characterization of the threshold and bifurcation behavior.

6.2. Threshold dynamics

The basic reproduction number of the full co-infection model is $\mathcal{R}_0 = \mathcal{R}_{0c}$, since CKD is non communicable and contributes no infectious secondary cases at the DFE; the corresponding next-generation matrix is block-triangular with a zero-CKD diagonal block. For the calibrated Indian baseline, $\mathcal{R}_0 = \mathcal{R}_{0c} \approx 2.84$, indicating that COVID-19 would invade and persist in a fully susceptible population. The long-run CKD prevalence is governed by a separate dimensionless invasion index

$$C_k = \frac{\lambda_k \Lambda(\psi + \zeta_k)}{\mu(\phi_k \psi - \gamma_h \zeta_k)}, \qquad \phi_k = \zeta_k + \mu_k + \mu, \qquad \psi = \gamma_h + \mu_h + \mu,$$

which evaluates to $C_k \approx 1.47$ under baseline conditions. We emphasize that C_k is not a basic reproduction number—it does not represent secondary cases generated by infectious contact—but is rather a dimensionless ratio that quantifies the accumulated long-run CKD prevalence under the constant non communicable hazard λ_k. The previous formulation $\mathcal{R}_0 = \max\{\mathcal{R}_{0c}, \mathcal{R}_{0k}\}$ has been replaced throughout the manuscript by $\mathcal{R}_0 = \mathcal{R}_{0c}$, with C_k tracked separately.

The DFE E_0 is locally asymptotically stable when $\mathcal{R}_0 < 1$ and unstable when $\mathcal{R}_0 > 1$, while the unique COVID-19 dominant boundary equilibrium E^* (with $I_k^* = I_{ck}^* = 0$) is locally asymptotically stable when $\mathcal{R}_{0c} > 1$, consistent with classical threshold theory.

Center manifold analysis confirms a forward (supercritical) bifurcation at $\mathcal{R}_{0c} = 1$, with the Castillo-Chavez and Song coefficients satisfying $a < 0$ and $b > 0$ [29], ruling out backward bifurcation entirely under the assumed parameter regime. This result has a strong analytical and public health implicatios: Reducing $\mathcal{R}_{0c}$ below unity is both necessary and sufficient to guarantee COVID-19's elimination from a disease-free starting state, with no stable subthreshold endemic state. This distinguishes the present model from COVID-19–tuberculosis co-infection frameworks, where latent reactivation can sustain endemic persistence even when $\mathcal{R}_0 < 1$ due to backward bifurcation [24, 25], and provides a strong analytical guarantee that intervention-based disease control is achievable without the ambiguity of bistable systems.

Scope and co-endemic state. The threshold $\mathcal{R}_0 = \mathcal{R}_{0c}$ characterizes invasion from the fully disease-free state E_0 only and governs the local asymptotic stability of E_0; it does not characterize persistence thresholds when both COVID-19 and CKD are simultaneously co-endemic. Numerical integration of the full system over 50 000 days from a range of biologically plausible initial conditions establishes the existence of a non-trivial co-endemic equilibrium with $I_c^* > 0$, $I_k^* > 0$, and $I_{ck}^* > 0$ simultaneously when $\mathcal{R}_{0c} > 1$ and $C_k > 1$. A complete analytical characterization of this co-endemic state is precluded by the bidirectional non-linear coupling of I_c, I_k, and I_{ck} and is identified as a direction for future work.

6.3. Calibration and sensitivity

The model was separately calibrated against two independent epidemiological datasets from India: Cumulative COVID-19 case data covering the period March 2020 to May 2021 [42], and annual CKD prevalence estimates spanning the full period 1990–2023 sourced from the Global Burden of Disease Study 2023 [43], achieving $R^2 > 0.999$ for each disease component independently. These calibrations were performed as separate fitting procedures against data from distinct time periods, not as a single joint fit; the parameters β_c, π, and γ_c were estimated from the cumulative COVID-19 trajectory, while λ_k (the per-capita non communicable CKD incidence rate) was estimated from the CKD prevalence series. Long-run CKD projections are qualitatively consistent with Global Burden of Disease estimates of approximately 115 million and 138 million prevalent CKD cases in India in 2017 and 2023 respectively [5, 43], providing external validation beyond the calibration window.

Normalized sensitivity analysis identifies β_c as the dominant positive driver of $\mathcal{R}_0$ (sensitivity index $\Upsilon_{\beta_c}^{\mathcal{R}_0} = +1.0000$), confirming that $\mathcal{R}_0$ is directly proportional to the COVID-19 transmission rate and that a 1% increase in β_c produces an equal 1% increase in the reproduction number (Figure 3). Vaccine efficacy ϵ_v carries the largest negative sensitivity index ($\Upsilon_{\epsilon_v}^{\mathcal{R}_0} = -1.2464$), making it the single most potent lever for threshold reduction—a 1% increase in vaccine efficacy reduces $\mathcal{R}_0$ by approximately 1.25%. The recovery rate γ_c is the second strongest suppressor ($\Upsilon_{\gamma_c}^{\mathcal{R}_0} = -0.6300$), confirming that both vaccine quality and clinical recovery speed are the primary structural targets for epidemic control in this population.

Global PRCC analysis (Figure 4), conducted using $N = 1000$ LHS realizations with each parameter varied uniformly within ±25% of its baseline value, reveals that the COVID-19 transmission rate β_c and the immunity waning rate π are the two dominant positive drivers of infection burden across all three infected compartments I_c, I_k, and I_{ck}. Specifically, β_c achieves PRCC values of +0.7332, +0.7283, and +0.7329 for I_c, I_k, and I_{ck}, respectively, while π yields values of +0.5416, +0.5455, and +0.5246, both consistently exceeding the strong influence threshold of 0.5 across all compartments. Vaccine efficacy ϵ_v dominates as the strongest suppressive parameter across all three infected compartments, with PRCC values of −0.9802, −0.9803, and −0.9795 for I_c, I_k, and I_{ck}, respectively, approaching −1.0 and identifying it as the most structurally influential parameter in suppressing infection across the entire model. While β_c ranks above π as the top positive driver in all three compartments, the strong and consistent influence of π across all compartments confirms that sustaining immune protection is nearly as critical as reducing transmission in the post-vaccination regime ; this conclusion holds within the ±25% uncertainty range used in the PRCC analysis (and was verified to remain stable under alternative ±15% and ±35% sampling windows and integration horizons of 250, 500, and 1 000 days). The hospitalization recovery rate γ_h exerts a consistent and significant negative influence across all compartments (PRCC values of −0.4372, −0.4304, and −0.4524 for I_c, I_k, and I_{ck} respectively), confirming that accelerating clinical recovery reduces the infection burden across the full disease spectrum. The CKD compartment remains sensitive to immunity and transmission dynamics through cross-disease coupling terms embedded in the system, and the response surfaces in Figure 5 confirm superadditive infection reductions when vaccination and hospitalization rates are elevated jointly, underscoring the structural complementarity of these two intervention mechanisms.

6.4. Optimal control results

Three time-dependent optimal controls were introduced into the baseline model: Vaccination (u_1), clinical management and hospitalization control (u_2), and enhanced hospitalization recovery (u_3). The controls are formulated to augment, rather than replace, the baseline rates: Vaccination becomes $\eta + \varepsilon_1 u_1$, hospitalization rates become $(1 + \varepsilon_2 u_2)\zeta_j$, and the recovery rate becomes $(1 + \varepsilon_3 u_3)\gamma_h$; with $u_i = 0$, the system reduces exactly to the uncontrolled baseline. Optimal conditions were derived via Pontryagin's maximum principle [31], and the resulting optimality system—comprising the controlled state equations (5.1), the adjoint system (5.3), the transversality conditions $\lambda_i(T) = 0$, and the projection formulae for u_1^*, u_2^*, and u_3^*—was solved numerically using the forward–backward sweep method with an RK4 scheme [32] over a 300-day intervention horizon.

Under the clinical management and hospitalization strategy (u_2–u_3), which activates the clinical management of infected compartments and enhanced hospitalization recovery while holding vaccination fixed at the baseline, the peak reductions relative to the uncontrolled scenario were 37% for I_c, 30% for I_k, 45.3% for I_{ck}, and 41.5% for H (Figure 6). These reductions arise structurally from two complementary mechanisms: u_2 increases removal from the infectious compartments I_c, I_k, and I_{ck} by scaling the hospitalization rates ζ_c, ζ_k, and ζ_{ck}, thereby shortening the effective infectious period in the community, while u_3 augments the recovery rate of hospitalized individuals from the baseline γ_h to $(1 + \varepsilon_3 u_3)\gamma_h$, accelerating clearance of the hospitalized class. The co-affected class I_{ck} exhibits the largest relative reduction under this strategy (45.3%), reflecting the dual pathway through which u_2 acts on this compartment: Directly through ζ_{ck}, and indirectly by reducing the infectious pool that drives new co-infections.

Under the vaccination-only strategy (u_1), which augments the effective vaccination rate above the background level η while holding the u_2–u_3 controls at zero, the peak reductions were 48.1% for I_c, 40.0% for I_k, 47.6% for I_{ck}, and 47.6% for H (Figure 7), outperforming the u_2–u_3 strategy across all compartments. Within the model structure, u_1 reduces the effective susceptible pool through the force of infection term, lowering incidence at the source rather than shortening infectiousness downstream. The co-affected class benefits disproportionately because CKD patients carry an immune modulation factor $\alpha < 1$, reducing their baseline COVID-19 acquisition rate; vaccination's protective effect therefore acts on a population whose net infection threshold is already modulated, amplifying the relative benefit of vaccination in this subgroup. The optimal vaccination control $u_1^*(t)$ maintains near-maximum effort ($u_1 \approx 1$) throughout the entire 300-day horizon (Figure 9(a)), consistent with the bang-bang switching structure predicted by Pontryagin's maximum principle: Since the susceptible pool $S(t)$ is of the order 10^9, the switching function $\psi_1(t) = \varepsilon_1(\lambda_1 - \lambda_2)S(t)/B_1$ remains positive throughout $[0, T]$, making maximum vaccination effort always cost-optimal.

Under the combined strategy (u_1, u_2, u_3), which activates all three controls simultaneously, peak reductions reached 59.3% for I_c, 53.8% for I_k, 62.7% for I_{ck}, and 54.9% for H (Figure 8), exceeding the arithmetic sum of individual strategy effects and demonstrating genuine superadditivity. The three controls act through complementary and hierarchically ordered pathways: u_1 prevents new infections by reducing the effective susceptible pool and lowering the force of infection; u_2 shortens the effective infectious period in the community by accelerating transfer from I_c, I_k, and I_{ck} to the hospitalized class; and u_3 accelerates recovery from hospitalization by enhancing the transition from H to R. Their simultaneous implementation therefore modifies both the incidence and the removal dynamics, producing greater reductions in the infection burden than isolated variation of either mechanism alone.

The temporal ordering of the optimal control profiles (Figure 9) is consistent with this hierarchical structure: u_3 begins declining first (after Day 220) as the hospitalized class $H(t)$ reduces, followed by u_2 (after Day 240) as the upstream infected compartments deplete, while u_1 is maintained at near-maximum throughout $[0, T]$ due to the persistently large susceptible pool. A robustness sweep over the cost weights $B_i \in \{25, 55, 100, 200\}$ and $A_4 \in \{10, 50, 100\}$, together with an insensitivity check on initial CKD-related compartments scaled by 0.5× and 2×, confirmed that the qualitative ordering combined > vaccination-only > (u_2–u_3) is preserved across all configurations, with peak reductions varying by less than ±6 percentage points.A consolidated quantitative comparison across all strategies is presented in Table 2.

Table 2. Percentage reductions in peak compartment sizes under each intervention strategy relative to the uncontrolled scenario.

Strategy	I_c (%)	I_k (%)	I_{ck} (%)	H (%)
u_2–u_3 strategy (u_2, u_3)	37.0	30.0	45.3	41.5
Vaccination only (u_1)	48.1	40.0	47.6	47.6
Combined (u_1, u_2, u_3)	59.3	53.8	62.7	54.9

6.5. Model limitations

The model assumes a homogeneous population, ignoring age, spatial, and socioeconomic heterogeneity, and does not incorporate healthcare capacity constraints, potentially overestimating the intervention's impact in resource-limited settings. Vaccine efficacy is treated as constant, and stochastic effects near threshold levels are neglected, while parameter uncertainty and out-of-sample validation are not addressed. The basic reproduction number $\mathcal{R}_0 = \mathcal{R}_{0c}$ characterizes invasion from the fully DFE only and does not govern persistence at the co-endemic state, whose existence is established numerically but not analytically. The CKD pathway is treated as a non communicable, irreversible process driven by a constant per-capita incidence rate λ_k that captures the net population-level effect of diabetes, hypertension, aging, and other non-transmission risk factors; this aggregate representation does not resolve the heterogeneous risk structure of CKD across diabetic, hypertensive, and elderly sub populations, nor does it explicitly model dialysis or transplant patients. The progression rate θ from acute COVID-19 to the co-affected class I_{ck} is interpreted as the rate of COVID-19-induced AKI rather than a transition to clinically established CKD (which, by definition, requires more than three months of sustained renal impairment); future work should disaggregate I_{ck} into separate AKI and established CKD compartments. The immunity waning rate π is fixed, structural assumptions may slightly underestimate reinfection in CKD populations, and uniform control cost weights ($B_i = 55$) may affect robustness—although the sensitivity sweep over weight choices and initial conditions reported above confirmed that the qualitative ordering of intervention strategies is preserved. Future work should incorporate heterogeneity, stochastic dynamics, time-varying immunity, healthcare capacity constraints, disaggregation of acute and chronic kidney compartments, and improved parameter estimation to enhance the real-world applicability.

6.6. Clinical implications

The forward bifurcation result ensures that reducing $\mathcal{R}_0 = \mathcal{R}_{0c}$ below unity eliminates COVID-19 from the disease-free state and, in conjunction with $C_k < 1$, also stabilizes the linearized CKD prevalence threshold, providing a clear target for public health planning, especially given the irreversible nature of CKD. Vaccine efficacy ϵ_v emerges as the most influential parameter, while waning immunity π significantly drives infection dynamics, highlighting the importance of booster vaccination—particularly for CKD patients with a reduced immune response. The combined intervention strategy achieves substantially greater reductions in co-infections and hospitalizations than single strategies, demonstrating strong synergistic benefits and supporting integrated approaches that combine vaccination, clinical management and hospitalization triage, and enhanced recovery. These interventions not only reduce transmission but also alleviate hospital burden, which is critical for high-risk CKD patients. Additionally, the sensitivity of CKD dynamics to waning COVID-19 immunity indicates that vaccination programs provide indirect benefits in reducing CKD burden, reinforcing the need for integrated infectious and chronic disease management strategies.

7. Conclusions

This study developed and rigorously analyzed a seven-compartment deterministic model for the co-dynamics of COVID-19 and chronic kidney disease (CKD), incorporating CKD irreversibility, an immune modulation factor $0 < \alpha \leq 1$, vaccine imperfection $(1-\varepsilon_v)$, bidirectional progression pathways θ and γ_{ck}, and a dimensionless H-recovery splitting fraction $p \in [0, 1]$ that preserves mass balance while respecting CKD irreversibility. The basic reproduction number $\mathcal{R}_0 = \mathcal{R}_{0c}$ was derived via the next-generation matrix method; since CKD is non-communicable, the long-run CKD prevalence is governed by the separate dimensionless invasion index C_k, which evaluates to $\mathcal{R}_0 \approx 2.84$ and $C_k \approx 1.47$ under the calibrated Indian baseline. Local and global asymptotic stability of the disease-free equilibrium E_0 were established for $\mathcal{R}_0 < 1$ and $C_k < 1$, and center manifold analysis confirmed a forward (supercritical) bifurcation at $\mathcal{R}_{0c} = 1$, ruling out backward bifurcation and guaranteeing that reducing $\mathcal{R}_0$ below unity is both necessary and sufficient for COVID-19 elimination. The model was validated against two independent Indian epidemiological datasets achieving $R^2 > 0.999$ for both disease components. Normalized sensitivity analysis identified vaccine efficacy ε_v as the dominant suppressor of $\mathcal{R}_0$ (index -1.2464), while global PRCC analysis confirmed that ε_v (PRCC ≈ -0.98 across all infected compartments) and transmission rate β_c are the most structurally influential parameters, with immunity waning π emerging as a critical secondary driver.

Three time-dependent optimal controls—vaccination $u_1(t)$, clinical management and hospitalization triage $u_2(t)$, and enhanced hospitalization recovery $u_3(t)$—were formulated via Pontryagin's Maximum Principle and solved numerically using the forward–backward sweep method over a 300-day horizon. The vaccination-only strategy achieved peak reductions of 48.1%, 40.0%, 47.6%, and 47.6% in I_c, I_k, I_{ck}, and H respectively, outperforming the clinical-management-and-hospitalization strategy (u_2, u_3: 37.0%, 30.0%, 45.3%, 41.5%), while the combined strategy (u_1–u_3) achieved the greatest reductions of 59.3%, 53.8%, 62.7%, and 54.9%, demonstrating genuine superadditivity through complementary mechanisms acting on both incidence and removal dynamics. These results establish that coordinated, multi-pronged interventions targeting high vaccine efficacy, sustained immune protection, and accelerated clinical management yield substantially greater reductions in co-infection

prevalence and hospitalization burden than isolated strategies, and that vaccination provides indirect benefits in reducing CKD burden through cross-disease coupling. Future work should address demographic heterogeneity, stochastic dynamics, time-varying vaccine efficacy, healthcare capacity constraints, disaggregation of the co-affected compartment into acute kidney injury and established CKD subgroups, and a complete analytical characterization of the co-endemic equilibrium.

Author contributions

Mallela Ankamma Rao: Conceptualization, methodology, software, validation, formal analysis, investigation, data curation, writing—original draft, writing—-review and editing, supervision; Emad K Jaradat: Conceptualization, methodology, formal analysis, investigation, resources, writing—review and editing, visualization, funding acquisition; Medisetty Padma Devi: Methodology, software, validation, formal analysis, data curation, writing—original draft, visualization; Prasantha Bharathi Dhandapani: Conceptualization, methodology, software, validation, formal analysis, investigation, resources, data curation, writing—original draft, writing—review and editing, visualization; Carlos Martin-Barreiro: Conceptualization, methodology, software, validation, formal analysis, investigation, resources, data curation, writing—original draft, writing—review and editing, visualization, supervision; Mohannad Al-Hmoud: Conceptualization, investigation, resources, writing—review and editing. All authors have read and approved the final version of the manuscript for publication.

Use of Generative-AI tools declaration

The authors declare that no Artificial Intelligence (AI) tools were used in the composition of this article.

Acknowledgments

This work was supported and funded by the Deanship of Scientific Research at Imam Mohammad Ibn Saud Islamic University (IMSIU) (grant number IMSIU-DDRSP2602).

Conflict of interest

The authors declare that they have no known competing financial interests or personal relationships that could have appeared to influence the work reported in this paper.

Availability of data and materials

The data that support the findings of this study are available from the corresponding author upon reasonable request.

References

1. World Health Organization, Tracking SARS-CoV-2 variants, 2021. Available from: https://www.who.int/activities/tracking-SARS-CoV-2-variants.

2. W. T. Harvey, A. M. Carabelli, B. Jackson, R. K. Gupta, E. C. Thomson, E. M. Harrison, et al., SARS-CoV-2 variants, spike mutations and immune escape, *Nat. Rev. Microbiol.*, **19** (2021), 409–424. https://doi.org/10.1038/s41579-021-00573-0
3. A. Telenti, E. B. Hodcroft, D. L. Robertson, The evolution and biology of SARS-CoV-2 variants, *Cold Spring Harb. Perspect. Med.*, **12** (2022), a041390. https://doi.org/10.1101/cshperspect.a041390
4. E. Callaway, Why a highly mutated coronavirus variant has scientists on alert, *Nature*, **620** (2023), 934. https://doi.org/10.1038/d41586-023-02656-9
5. P. B. Mark, L. K. Stafford, M. E. Grams, H. Aalruz, S. Abd ElHafeez, A. A. Abdelgalil, et al., Global, regional, and national burden of chronic kidney disease in adults, 1990–2023, and its attributable risk factors: a systematic analysis for the Global Burden of Disease Study 2023, *Lancet*, **406** (2025), 2461–2482. https://doi.org/10.1016/S0140-6736(25)01853-7
6. B. Bikbov, C. A. Purcell, A. S. Levey, M. Smith, A. Abdoli, M. Abebe, et al., Global, regional, and national burden of chronic kidney disease, 1990–2017: a systematic analysis for the Global Burden of Disease Study 2017, *Lancet*, **395** (2020), 709–733. https://doi.org/10.1016/S0140-6736(20)30045-3
7. G. Eknoyan, T. Hostetter, G. L. Bakris, L. Hebert, A. S. Levey, H. H. Parving, et al., Proteinuria and other markers of chronic kidney disease: a position statement of the national kidney foundation (NKF) and the national institute of diabetes and digestive and kidney diseases (NIDDK), *Am. J. Kidney Dis.*, **42** (2003), 617–622. https://doi.org/10.1016/S0272-6386(03)00826-6
8. R. Borg, N. Carlson, J. Søndergaard, F. Persson, The growing challenge of chronic kidney disease: an overview of current knowledge, *Int. J. Nephrol.*, **2023** (2023), 9609266. https://doi.org/10.1155/2023/9609266
9. P. E. Stevens, S. B. Ahmed, J. J. Carrero, B. Foster, A. Francis, R. K. Hall, et al., KDIGO 2024 clinical practice guideline for the evaluation and management of chronic kidney disease, *Kidney Int.*, **105** (2024), S117–S314. https://doi.org/10.1016/j.kint.2023.10.018
10. C. W. Mende, Chronic kidney disease and SGLT2 inhibitors: a review of the evolving treatment landscape, *Adv. Ther.*, **39** (2024), 148–164. https://doi.org/10.1007/s12325-021-01994-2
11. S. S. Jdiaa, R. Mansour, A. El Alayli, A. Gautam, P. Thomas, R. A. Mustafa, COVID-19 and chronic kidney disease: an updated overview of reviews, *J. Nephrol.*, **35** (2022), 69–85. https://doi.org/10.1007/s40620-021-01206-8
12. E. Y. M. Chung, S. C. Palmer, P. Natale, A. Krishnan, T. E. Cooper, V. M. Saglimbene, et al., Incidence and outcomes of COVID-19 in people with CKD: a systematic review and meta-analysis, Am. *J. Kidney Dis.*, **78** (2021), 804–815. https://doi.org/10.1053/j.ajkd.2021.07.003
13. V. Ambalarajan, A. R. Mallela, V. Sivakumar, P. B. Dhandapani, V. Leiva, C. Martin-Barreiro, et al., A six-compartment model for COVID-19 with transmission dynamics and public health strategies, *Sci. Rep.*, **14** (2024), 22226. https://doi.org/10.1038/s41598-024-72487-9
14. Y. Zhang, Y. Zhao, J. Wang, X. Zheng, D. Xu, J. Lv, et al., Long-term renal outcomes of patients with COVID-19: a meta-analysis of observational studies, *J. Nephrol.*, **36** (2023), 2441–2456. https://doi.org/10.1007/s40620-023-01731-8

15. I. Chen, L. Chang, C. Ho, J. Wu, Y. Tsai, C. Lin, et al., Association between COVID-19 and the development of chronic kidney disease in patients without initial acute kidney injury, *Sci. Rep.*, **15** (2025), 10924. https://doi.org/10.1038/s41598-025-96032-4

16. H. Rabb, Kidney diseases in the time of COVID-19: major challenges to patient care, *J. Clin. Invest.*, **130** (2020), 2749–2751. https://doi.org/10.1172/JCI138871

17. P. van den Driessche, J. Watmough, Reproduction numbers and sub-threshold endemic equilibria for compartmental models of disease transmission, *Math. Biosci.*, **180** (2002), 29–48. https://doi.org/10.1016/S0025-5564(02)00108-6

18. O. Diekmann, J. A. P. Heesterbeek, M. G. Roberts, The construction of next-generation matrices for compartmental epidemic models, *J. R. Soc. Interface*, **7** (2010), 873–885. https://doi.org/10.1098/rsif.2009.0386

19. Z. Liu, G. Wan, B. A. Prakash, M. S. Y. Lau, W. Jin, A review of graph neural networks in epidemic modeling, *Proceedings of the 30th ACM SIGKDD Conference on Knowledge Discovery and Data Mining*, 2024, 6577–6587. https://doi.org/10.1145/3637528.3671455

20. I. Takaidza, O. D. Makinde, O. K. Okosun, Computational modelling and optimal control of Ebola virus disease with non-linear incidence rate, *J. Phys.: Conf. Ser.*, **818** (2017), 012003. https://doi.org/10.1088/1742-6596/818/1/012003

21. O. Kiseleva, S. Yakovlev, O. Prytomanova, O. Kuzenkov, Mathematical modeling of regional infectious disease dynamics based on extended compartmental models, *Computation*, **13** (2025), 187. https://doi.org/10.3390/computation13080187

22. S. Marino, I. B. Hogue, C. J. Ray, D. E. Kirschner, A methodology for performing global uncertainty and sensitivity analysis in systems biology, *J. Theor. Biol.*, **254** (2008), 178–196. https://doi.org/10.1016/j.jtbi.2008.04.011

23. D. S. Mgonja, A. Hugo, A. Hassan, O. D. Makinde, Mathematical modeling and analysis of COVID-19 and typhoid fever co-dynamics with treatment, *Sci. Rep.*, **15** (2025), 33206. https://doi.org/10.1038/s41598-024-82955-x

24. J. O. Akanni, S. Ajao, S. F. Abimbade, Fatmawati, Dynamical analysis of COVID-19 and tuberculosis co-infection using mathematical modelling approach, *Math. Model. Control*, **4** (2024), 208–229. https://doi.org/10.3934/mmc.2024018

25. K. G. Mekonen, L. L. Obsu, Mathematical modeling and analysis for the co-infection of COVID-19 and tuberculosis, *Heliyon*, **8** (2022), e11195. https://doi.org/10.1016/j.heliyon.2022.e11195

26. M. Ankamma Rao, E. K. Jaradat, M. Padma Devi, P. B. Dhandapani, R. M. Nalule, M. Al-Hmoud, Modeling COVID-19 pneumonia and COVID-associated pulmonary aspergillosis: sensitivity analysis and optimal control, *BMC Infect. Dis.*, **25** (2025), 1192. https://doi.org/10.1186/s12879-025-11606-x

27. M. A. Hye, M. H. A. Biswas, M. F. Uddin, M. M. Rahman, A mathematical model for the transmission of co-infection with COVID-19 and kidney disease, *Sci. Rep.*, **14** (2024), 5680. https://doi.org/10.1038/s41598-024-56399-2

28. D. Gibertoni, C. Reno, P. Rucci, M. P. Fantini, A. Buscaroli, G. Mosconi, et al., COVID-19 incidence and mortality in non-dialysis chronic kidney disease patients, *PLoS ONE*, **16** (2021), e0254525. https://doi.org/10.1371/journal.pone.0254525
29. C. Castillo-Chavez, B. Song, Dynamical models of tuberculosis and their applications, *Math. Biosci. Eng.*, **1** (2004), 361–404. https://doi.org/10.3934/mbe.2004.1.361
30. N. Chitnis, J. M. Hyman, J. M. Cushing, Determining important parameters in the spread of malaria through the sensitivity analysis of a mathematical model, *Bull. Math. Biol.*, **70** (2008), 1272–1296. https://doi.org/10.1007/s11538-008-9299-0
31. L. S. Pontryagin, V. G. Boltyanskii, R. V. Gamkrelidze, E. F. Mishchenko, *The mathematical theory of optimal processes*, Boca Raton, FL: CRC Press, 2018. https://doi.org/10.1201/9780203749319
32. S. Lenhart, J. T. Workman, *Optimal control applied to biological models*, Boca Raton, FL: Chapman & Hall/CRC, 2007. https://doi.org/10.1201/9781420011418
33. K. Jain, A. Bhattacharjee, S. Krishnamurhty, Mathematical analysis of COVID-19 and TB co-infection dynamics with optimal control, *Model. Earth Syst. Environ.*, **11** (2025), 65. https://doi.org/10.1007/s40808-024-02197-8
34. S. Kurmi, U. Chouhan, A multicompartment mathematical model to study the dynamic behaviour of COVID-19 using vaccination as control parameter, *Nonlinear Dyn.*, **109** (2022), 2185–2201. https://doi.org/10.1007/s11071-022-07591-4
35. S. Bugalia, J. P. Tripathi, H. Wang, Estimating the time-dependent effective reproduction number and vaccination rate for COVID-19 in the USA and India, *Math. Biosci. Eng.*, **20** (2023), 4673–4689. https://doi.org/10.3934/mbe.2023216
36. R. K. Rai, S. Khajanchi, P. K. Tiwari, E. Venturino, A. K. Misra, Impact of social media advertisements on the transmission dynamics of COVID-19 pandemic in India, *J. Appl. Math. Comput.*, **68** (2022), 19–44. https://doi.org/10.1007/s12190-021-01507-y
37. S. J. Schrauben, H. Chen, E. Lin, C. Jepson, W. Yang, J. J. Scialla, et al., Hospitalizations among adults with chronic kidney disease in the United States: a cohort study, *PLOS Med.*, **17** (2020), e1003470. https://doi.org/10.1371/journal.pmed.1003470
38. Y. Gao, Y. Chen, M. Liu, S. Shi, J. Tian, Impacts of immunosuppression and immunodeficiency on COVID-19: a systematic review and meta-analysis, *J. Infect.*, **81** (2020), e93–e95. https://doi.org/10.1016/j.jinf.2020.05.017
39. V. P. Bajiya, S. Bugalia, J. P. Tripathi, Mathematical modeling of COVID-19: impact of non-pharmaceutical interventions in India, *Chaos*, **30** (2020), 113143. https://doi.org/10.1063/5.0021353
40. F. Shahbazi, A. Doosti-Irani, A. Soltanian, J. Poorolajal, Global forecasting of chronic kidney disease mortality rates and numbers with the generalized additive model, *BMC Nephrol.*, **25** (2024), 286. https://doi.org/10.1186/s12882-024-03720-w
41. Y. Cheng, R. Luo, K. Wang, M. Zhang, Z. Wang, L. Dong, et al., Kidney disease is associated with in-hospital death of patients with COVID-19, *Kidney Int.*, **97** (2020), 829–838. https://doi.org/10.1016/j.kint.2020.03.005

42. COVID-19 India, COVID-19 India dataset, 2024. Available from: https://data.covid19india.org/.
43. Institute for Health Metrics and Evaluation (IHME), GBD Results Tool, 2025. Available from: https://vizhub.healthdata.org/gbd-results/.
44. D. R. Powell, J. Fair, R. J. LeClaire, L. M. Moore, D. Thompson, Sensitivity analysis of an infectious disease model, ISDC 2005, 2005. Available from: https://proceedings.systemdynamics.org/2005/proceed/papers/LECLA330.pdf.
45. J. Wu, R. Dhingra, M. Gambhir, J. V. Remais, Sensitivity analysis of infectious disease models: methods, advances and their application, *J. R. Soc. Interface*, **10** (2013), 20121018. https://doi.org/10.1098/rsif.2012.1018
46. M. Martcheva, *An introduction to mathematical epidemiology*, New York, NY: Springer, 2015. https://doi.org/10.1007/978-1-4899-7612-3
47. Z. Zhang, R. Gul, A. Zeb, Global sensitivity analysis of COVID-19 mathematical model, *Alex. Eng. J.*, **60** (2020), 565–572. https://doi.org/10.1016/j.aej.2020.09.035
48. V. Ambalarajan, A. R. Mallela, P. B. Dhandapani, V. Sivakumar, V. Leiva, C. Castro, Multi-strain COVID-19 dynamics with vaccination strategies: mathematical modeling and case study, *Alex. Eng. J.*, **119** (2025), 665–684. https://doi.org/10.1016/j.aej.2025.01.105
49. P. Hartman, Ordinary differential equations (2nd ed.), *Society for Industrial and Applied Mathematics*, 2002. https://doi.org/10.1137/1.9780898719222
50. J. P. LaSalle, *The stability of dynamical systems*, Philadelphia, PA: Society for Industrial and Applied Mathematics, 1976.

Appendix

Appendix A

A1. Proof of Theorem 3.1

Proof. We establish the positivity and boundedness for Submodel (3.1).

Positivity.

- At $S = 0$: $\dot{S} = \Lambda + \pi R \geq \Lambda > 0$, so $S(t) \geq 0$.
- At $V = 0$: $\dot{V} = \eta S \geq 0$, so $V(t) \geq 0$.
- At $I_c = 0$: $\dot{I}_c = \beta_c H[S + (1 - \epsilon_v)V]/N \geq 0$.
- At $H = 0$: $\dot{H} = \zeta_c I_c \geq 0$.
- At $R = 0$: $\dot{R} = \gamma_c I_c + \gamma_h H \geq 0$.

Hence $\mathbb{R}^5_{\geq 0}$ is forward-invariant.

Boundedness. Summing the five equations, giving

$$\dot{N} = \Lambda - \mu N - \mu_c I_c - \mu_h H \leq \Lambda - \mu N.$$

By the comparison principle, $N(t) \leq \Lambda/\mu + (N(0) - \Lambda/\mu)e^{-\mu t}$, so $\limsup_{t\to\infty} N(t) \leq \Lambda/\mu$ and Ω is positively invariant. □

A2. Proof of Theorem 3.2

Proof. The Jacobian of Submodel (3.1) at E_{0c} is

$$J(E_{0c}) = \begin{pmatrix} -(\eta+\mu) & 0 & -A & -A & \pi \\ \eta & -\mu & -B & -B & 0 \\ 0 & 0 & A-\phi & A & 0 \\ 0 & 0 & \zeta_c & -\psi & 0 \\ 0 & 0 & \gamma_c & \gamma_h & -(\mu+\pi) \end{pmatrix},$$

where

$$A = \frac{\beta_c(S^0 + (1-\epsilon_v)V^0)}{N^0} = \frac{\beta_c(\mu + \eta(1-\epsilon_v))}{\eta+\mu}, \qquad B = \frac{(1-\epsilon_v)\beta_c\eta}{\eta+\mu},$$
$$\phi = \zeta_c + \gamma_c + \mu_c + \mu, \qquad \psi = \gamma_h + \mu_h + \mu.$$

The block-triangular characteristic polynomial factorizes as

$$(\lambda + \eta + \mu)(\lambda + \mu)(\lambda + \mu + \pi) \cdot \det(M - \lambda I) = 0,$$

where M denotes the 2×2 infected sub-block

$$M = \begin{pmatrix} A-\phi & A \\ \zeta_c & -\psi \end{pmatrix},$$

with the trace $A - \phi - \psi$ and the determinant $-(A-\phi)\psi - A\zeta_c = \phi\psi - A(\psi + \zeta_c)$. Both eigenvalues of M have negative real parts if and only if $\mathrm{tr}(M) < 0$ and $\det(M) > 0$, which together reduce to $\mathcal{R}_{0c} < 1$, where

$$\mathcal{R}_{0c} = \frac{A(\psi+\zeta_c)}{\phi\psi} = \frac{\beta_c(\mu + \eta(1-\epsilon_v))(\psi+\zeta_c)}{(\eta+\mu)\phi\psi}.$$

Therefore E_{0c} is locally asymptotically stable when $\mathcal{R}_{0c} < 1$ and unstable when $\mathcal{R}_{0c} > 1$. □

A3. Proof of Theorem 3.3

Proof. We apply the method of Castillo-Chavez et al. [29] with $X = (S, V, R)$, $Z = (I_c, H)$. Then $G(X, \mathbf{0}) = \mathbf{0}$. **Condition (H1).** Setting $I_c = H = 0$, the reduced system is

$$\dot{S} = \Lambda - (\eta+\mu)S + \pi R, \quad \dot{V} = \eta S - \mu V, \quad \dot{R} = -(\mu+\pi)R.$$

We write

$$\frac{dS}{dt} + (\eta+\mu)S = \Lambda + \pi R(t).$$

This is a first-order linear ordinary differential equation with forcing $\Lambda + \pi R(t) \to \Lambda$ exponentially as $t \to \infty$ (since $R(t) \to 0$ exponentially). The integrating factor solution $S(t) = e^{-(\eta+\mu)t}[S(0) + \int_0^t e^{(\eta+\mu)s}(\Lambda + \pi R(s))\,\mathrm{d}s]$ converges to $\Lambda/(\eta+\mu) = S^0$ as $t \to \infty$ by standard asymptotic analysis [49]. Substituting $S \to S^0$ into the V-equation gives $V(t) \to \eta S^0/\mu = V^0$. Hence $X(t) \to X^0$ and (H1) is satisfied.

Condition (H2). With $\phi = \zeta_c + \gamma_c + \mu_c + \mu$ and $f = \beta_c(S^0 + (1-\epsilon_v)V^0)/N^0$, the Jacobian $A = D_Z G(E_{0c})$ gives

$$\hat{G}(X,Z) = AZ - G(X,Z) = \begin{pmatrix} \beta_c(I_c + H)\left[\dfrac{S^0 + (1-\epsilon_v)V^0}{N^0} - \dfrac{S + (1-\epsilon_v)V}{N}\right] \\ 0 \end{pmatrix}.$$

We must show that the bracket is non-negative on Ω_c.

From the S-equation, $\dot{S} \le \Lambda + \pi R - (\eta+\mu)S \le \Lambda + \pi N^0 - (\eta+\mu)S$, since $R \le N \le N^0$ in Ω_c. The comparison principle gives $S(t) \le \tilde{S}(t)$, where $\tilde{S}$ solves the linear ordinary differential equation $\dot{\tilde{S}} = \Lambda + \pi N^0 - (\eta+\mu)\tilde{S}$. For DFE-consistent initial data ($S(0) \le S^0$, $R(0) = 0$), the solution satisfies $S(t) \le S^0$ for all $t \ge 0$ by monotone comparison. Similarly, from $\dot{V} = \eta S - \mu V \le \eta S^0 - \mu V$, the comparison principle yields $V(t) \le \eta S^0/\mu = V^0$. Combining, $S + (1-\epsilon_v)V \le S^0 + (1-\epsilon_v)V^0$. Since $N(t) \le N^0$ in Ω_c and $S^0 + V^0 = N^0$ at the DFE, we have

$$\frac{S + (1-\epsilon_v)V}{N} \le \frac{S^0 + (1-\epsilon_v)V^0}{N^0},$$

so $\hat{G}(X,Z) \ge \mathbf{0}$ throughout Ω_c.

Both (H1) and (H2) hold, so E_{0c} is globally asymptotically stable in Ω_c when $\mathcal{R}_{0c} < 1$. □

A4. Proof of Theorem 3.4

Proof. Relabel $x_1 = S$, $x_2 = V$, $x_3 = I_c$, $x_4 = H$, and $x_5 = R$. The corrected submodel has $\phi = \zeta_c + \gamma_c + \mu_c + \mu$ and $\dot{x}_5 = \gamma_c x_3 + \gamma_h x_4 - (\mu + \pi)x_5$.

Take β_c as bifurcation parameter; let β_c^* satisfy $\mathcal{R}_{0c} = 1$. By Theorem 3.2, $J(E_{0c}, \beta_c^*)$ has a simple zero eigenvalue and all other eigenvalues with strictly negative real parts. Let $w = (w_1, \ldots, w_5)^T$ and $v = (v_1, \ldots, v_5)$ be the right and left eigenvectors normalized by $vw = 1$ ($w_3, v_3 > 0$).

The relevant non-zero second derivatives, computed with the explicit $1/N^0$ scaling, are:

$$\frac{\partial^2 f_3}{\partial x_1 \partial x_3} = \frac{\beta_c^*}{N^0}, \quad \frac{\partial^2 f_3}{\partial x_2 \partial x_3} = \frac{(1-\epsilon_v)\beta_c^*}{N^0}, \quad \frac{\partial^2 f_3}{\partial x_3 \partial \beta_c} = \frac{x_1^0 + (1-\epsilon_v)x_2^0}{N^0}.$$

Substituting into the Castillo-Chavez–Song formulas, we have

$$a = -\frac{2v_3 w_1 w_3 \beta_c^* \phi(\eta+\mu)}{\Lambda} < 0, \qquad b = v_3 w_3 \cdot \frac{x_1^0 + (1-\epsilon_v)x_2^0}{N^0} \cdot \phi > 0.$$

Since $a < 0$ and $b > 0$, the bifurcation at $\mathcal{R}_{0c} = 1$ is forward; E_c^* is locally asymptotically stable for $\mathcal{R}_{0c} > 1$ and no backward bifurcation occurs. □

Appendix B

B1. Proof of Theorem 3.5

Proof. The CKD-only submodel is the three-compartment system in (S, I_k, H), with the COVID-19 specific classes V and R removed, and with the H-recovery flow returning entirely to I_k ($p = 0$ in Section 2) splitting:

$$\dot{S} = \Lambda - \lambda_k S - \mu S, \quad \dot{I}_k = \lambda_k S + \gamma_h H - \phi_k I_k, \quad \dot{H} = \zeta_k I_k - \psi H,$$

with $\phi_k = \zeta_k + \mu_k + \mu$, $\psi = \gamma_h + \mu_h + \mu$.

Positivity. At $S = 0$: $\dot{S} = \Lambda > 0$. At $I_k = 0$: $\dot{I}_k = \lambda_k S + \gamma_h H \geq 0$ (the $+\gamma_h H$ inflow is the back-flow from hospitalized CKD-only patients, respecting CKD's irreversibility. At $H = 0$: $\dot{H} = \zeta_k I_k \geq 0$. Hence $\mathbb{R}^3_{\geq 0}$ is forward-invariant.

Boundedness. Adding the three equations (the internal transfer $\gamma_h H$ between H and I_k cancels exactly), we have

$$\dot{N} = \Lambda - \mu N - \mu_k I_k - \mu_h H \leq \Lambda - \mu N.$$

By Grönwall, $\limsup_{t\to\infty} N(t) \leq \Lambda/\mu$, and Ω_k is positively invariant. □

B2. Proof of Theorem 3.6

Proof. Here, $E_{0k} = (\Lambda/\mu, 0, 0)$ is the linearized CKD-free reference state, not a true equilibrium of the nonlinear flow when $\lambda_k > 0$. The stability statement below concerns the linearized dynamics around $I_k = H = 0$.

The Jacobian of the three-compartment submodel at E_{0k} is

$$J(E_{0k}) = \begin{pmatrix} -(\mu + \lambda_k) & 0 & 0 \\ \lambda_k & -\phi_k & \gamma_h \\ 0 & \zeta_k & -\psi \end{pmatrix}.$$

The first eigenvalue is $\lambda_1 = -(\mu + \lambda_k) < 0$. The remaining 2×2 infected sub-block has the trace $-(\phi_k + \psi) < 0$ and the determinant $\phi_k\psi - \gamma_h\zeta_k$ (the $-\gamma_h\zeta_k$ correction arises from the $H \to I_k$ back-flow). Both eigenvalues from this block have negative real parts if and only if $\phi_k\psi - \gamma_h\zeta_k > 0$.

The CKD invasion index, computed with $S^0 = \Lambda/\mu$ (vaccination η is absent in the CKD-only submodel), is

$$C_k = \frac{\lambda_k \Lambda(\psi + \zeta_k)}{\mu(\phi_k\psi - \gamma_h\zeta_k)}.$$

The next-generation linearization gives $\lambda_5 = \phi_k(C_k - 1)$, so E_{0k} is locally asymptotically stable if and only if $C_k < 1$ and unstable if and only if $C_k > 1$. We re-emphasize that C_k is a dimensionless invasion index, not a basic reproduction number, since CKD is non communicable. □

B3. Proof of Theorem 3.7

Proof. We split this into two cases.

Case 1: $\lambda_k = 0$. With no inflow into I_k, the configuration $(\Lambda/\mu, 0, 0)$ is a true equilibrium. The S-equation $\dot{S} = \Lambda - \mu S$ gives $S(t) \to \Lambda/\mu$ exponentially. The (I_k, H) subsystem

$$\dot{I}_k = \gamma_h H - \phi_k I_k, \quad \dot{H} = \zeta_k I_k - \psi H,$$

has a system matrix with eigenvalues having negative real parts if $\phi_k\psi > \gamma_h\zeta_k$, which holds in the calibrated regime. Defining the Lyapunov function that $L = I_k + (\zeta_k/\psi)H$ and differentiating shows $\dot{L} \leq 0$ with equality only at $I_k = H = 0$. By Laselle [50], every trajectory converges to E_{0k}, which is therefore globally asymptotically stable in Ω_k.

Case 2: $\lambda_k > 0$. Now $\dot{I}_k|_{I_k=H=0} = \lambda_k S > 0$ when $S > 0$, so E_{0k} is not a fixed point of the dynamics. We show convergence to the unique CKD endemic equilibrium E_k^* (established in Theorem 3.8) via the Poincaré–Bendixson theorem applied to the (I_k, H)-plane. Specifically:

- Ω_k is compact and positively invariant (Theorem 3.5).
- By comparison principle reasoning applied to $\dot{S} \leq \Lambda - \mu S$, and $\limsup_{t\to\infty} S(t) \leq \Lambda/\mu$, the S enters and remains in a bounded set.
- The reduced two-dimensional flow in (I_k, H) has the divergence $-\phi_k - \psi < 0$, so by the Bendixson–Dulac criterion, no closed orbits exist.
- By the Poincaré–Bendixson theorem, every trajectory converges either to an equilibrium or to a closed orbit. Closed orbits are excluded, so the trajectories converge to the unique interior equilibrium E_k^* when $C_k > 1$ (the existence and local stability are established in Theorem 3.8).

This establishes the global convergence claim. □

B4. Proof of Theorem 3.8

Proof. Adopt the relabelling $x_1 = S$, $x_2 = I_k$, and $x_3 = H$ for the three-compartment submodel:

$$\dot{x}_1 = \Lambda - \lambda_k x_1 - \mu x_1, \quad \dot{x}_2 = \lambda_k x_1 + \gamma_h x_3 - \phi_k x_2, \quad \dot{x}_3 = \zeta_k x_2 - \psi x_3.$$

Take λ_k as bifurcation parameter; let λ_k^* satisfy $C_k = 1$, in which case

$$\lambda_k^* = \frac{\mu(\phi_k\psi - \gamma_h\zeta_k)}{\Lambda(\psi + \zeta_k)}.$$

By Theorem 3.6, $J(E_{0k}, \lambda_k^*)$ has a simple zero eigenvalue and all other eigenvalues with negative real parts. Castillo-Chavez and Song [29] applies.

The right-hand sides f_2 and f_3 are linear in the state variables for fixed λ_k; the only nonlinearity is the bilinear product $\lambda_k x_1$. Consequently, all pure spatial second derivatives $\partial^2 f_k/\partial x_i \partial x_j$ vanish at (E_{0k}, λ_k^*), giving the leading Castillo-Chavez–Song coefficient

$$a = 0.$$

Because $a = 0$ (a structural consequence of CKD being non communicable; the bilinear βIS nonlinearity that yields $a \neq 0$ in infectious disease models is absent here), we determine the bifurcation direction by computing E_k^* explicitly. Setting all derivatives to zero, we have

$$S^* = \frac{\Lambda}{\lambda_k + \mu}, \qquad H^* = \frac{\zeta_k I_k^*}{\psi}, \qquad I_k^* = \frac{\lambda_k S^* \psi}{\phi_k\psi - \gamma_h\zeta_k}.$$

Substituting S^* and using the definition of C_k, we have

$$I_k^* = \frac{\Lambda(\psi + \zeta_k)}{(\lambda_k + \mu)(\phi_k\psi - \gamma_h\zeta_k)} \cdot \mu(C_k - 1) \propto (C_k - 1).$$

Therefore $I_k^* > 0 \iff C_k > 1$, $I_k^* = 0$ at $C_k = 1$, and I_k^* is a continuous strictly increasing function of C_k near the critical value. The bifurcation is forward (supercritical), E_k^* inherits local asymptotic stability from E_{0k} via the exchange of stability principle, and no backward bifurcation occurs. □

Appendix C

C1. Proof of Theorem 3.9

Proof. **Positivity.** By contradiction, suppose that some variable first reaches zero at $t^* > 0$ with a strictly negative derivative. Let us examine each boundary:
• $S(t^*) = 0$: $\dot{S} = \Lambda + \pi R(t^*) \geq \Lambda > 0$.
• $V(t^*) = 0$: $\dot{V} = \eta S \geq 0$.
• $I_c(t^*) = 0$: $\dot{I}_c = \beta_c(I_{ck} + H)(S + (1 - \epsilon_v)V)/N \geq 0$.
• $I_k(t^*) = 0$: $\dot{I}_k = \lambda_k S + \gamma_{ck} I_{ck} + (1 - p)\gamma_h H \geq 0$ (the $(1 - p)\gamma_h H$ inflow is the H-recovery back-flow).
• $I_{ck}(t^*) = 0$: $\dot{I}_{ck} = \alpha\beta_c(I_c + H)I_k/N + \theta I_c \geq 0$.
• $H(t^*) = 0$: $\dot{H} = \zeta_c I_c + \zeta_k I_k + \zeta_{ck} I_{ck} \geq 0$.
• $R(t^*) = 0$: $\dot{R} = \gamma_c I_c + p\gamma_h H \geq 0$.
Each yields a contradiction; $\mathbb{R}^7_{\geq 0}$ is forward-invariant.
Boundedness. Summing ($p\gamma_h H + (1 - p)\gamma_h H = \gamma_h H$ matches the outflow from H) and gives:

$$\dot{N} = \Lambda - \mu N - \mu_c I_c - \mu_k I_k - \mu_{ck} I_{ck} - \mu_h H \leq \Lambda - \mu N.$$

Grönwall yields $\limsup_{t\to\infty} N(t) \leq \Lambda/\mu$, and Ω is positively invariant. □

C2. Proof of Theorem 3.10

Proof. At the DFE, the prefactor $I_c + I_{ck} + H$ in the force of infection terms vanishes, so the partial derivatives of $\beta_c(I_c + I_{ck} + H)Y/N$ with respect to S, V, I_k, or R are zero, while differentiation with respect to I_c, I_{ck}, or H yields the non-zero value $\beta_c Y^0/N^0$. Setting

$$A := \frac{\beta_c(S^0 + (1 - \epsilon_v)V^0)}{N^0} = \frac{\beta_c(\mu + \eta(1 - \epsilon_v))}{\eta + \mu}, \qquad B := \frac{\beta_c(1 - \epsilon_v)V^0}{N^0} = \frac{\beta_c(1 - \epsilon_v)\eta}{\eta + \mu},$$

and ordering the state vector as $(S, V, I_c, I_k, I_{ck}, H, R)^\top$, direct computation of every partial derivative of system (2.1) at E_0 gives

$$J(E_0) = \begin{pmatrix} -(\eta + \mu + \lambda_k) & 0 & -\frac{\beta_c S^0}{N^0} & 0 & -\frac{\beta_c S^0}{N^0} & -\frac{\beta_c S^0}{N^0} & \pi \\ \eta & -\mu & -B & 0 & -B & -B & 0 \\ 0 & 0 & A - \phi & 0 & A & A & 0 \\ \lambda_k & 0 & 0 & -\phi_k & \gamma_{ck} & (1 - p)\gamma_h & 0 \\ 0 & 0 & \theta & 0 & -\phi_{ck} & 0 & 0 \\ 0 & 0 & \zeta_c & \zeta_k & \zeta_{ck} & -\psi & 0 \\ 0 & 0 & \gamma_c & 0 & 0 & p\gamma_h & -(\mu + \pi) \end{pmatrix},$$

where $\phi = \theta + \zeta_c + \gamma_c + \mu_c + \mu$, $\phi_k = \zeta_k + \mu_k + \mu$, $\phi_{ck} = \zeta_{ck} + \gamma_{ck} + \mu_{ck} + \mu$, and $\psi = \gamma_h + \mu_h + \mu$.

The characteristic polynomial factorizes as

$$\det(J(E_0) - \lambda I_7) = (-(\eta + \mu + \lambda_k) - \lambda)(-\mu - \lambda)(-(\mu + \pi) - \lambda)(-\phi_k - \lambda)\det(M - \lambda I_3),$$

where M is the infected sub-block governing (I_c, I_{ck}, H) as follows:

$$M = \begin{pmatrix} A - \phi & A & A \\ \theta & -\phi_{ck} & 0 \\ \zeta_c & \zeta_{ck} & -\psi \end{pmatrix}.$$

The four scalar factors immediately yield four strictly negative eigenvalues $\lambda_1 = -(\eta+\mu+\lambda_k)$, $\lambda_2 = -\mu$, and $\lambda_3 = -(\mu + \pi)$, $\lambda_4 = -\phi_k$.

The remaining three eigenvalues are the roots of $\det(M - \lambda I_3) = 0$. Expanding the determinant gives the characteristic polynomial $\lambda^3 + c_2\lambda^2 + c_1\lambda + c_0 = 0$ with the constant term $c_0 = \phi\,\phi_{ck}\,\psi\,(1 - \mathcal{R}_{0c})$, where

$$\mathcal{R}_{0c} = \frac{\beta_c(\mu + \eta(1 - \epsilon_v))(\psi + \zeta_c)}{(\eta + \mu)\phi\psi} = \frac{A(\psi + \zeta_c)}{\phi\psi},$$

is the basic reproduction number derived in Section 3.3.1 via the next-generation matrix. The remaining coefficients $c_2 = \phi+\phi_{ck}+\psi-A$ and $c_1 = \phi\phi_{ck}+\phi\psi+\phi_{ck}\psi-A(\phi_{ck}+\psi+\zeta_c)-A\theta-A\zeta_{ck}$ are positive whenever $\mathcal{R}_{0c} < 1$, and the Routh–Hurwitz conditions $c_0, c_1, c_2 > 0$, together with $c_1c_2 > c_0$, are then satisfied, so all three roots of M have strictly negative real parts. Conversely, when $\mathcal{R}_{0c} > 1$, the constant term c_0 becomes negative, forcing at least one positive real root and hence the instability of E_0.

Therefore E_0 is locally asymptotically stable when $\mathcal{R}_0 = \mathcal{R}_{0c} < 1$ and unstable when $\mathcal{R}_{0c} > 1$. □

C3. Proof of Theorem 3.11

Proof. Define $\mathcal{L} = \ell_1 I_c + \ell_2 I_k + \ell_3 I_{ck} + \ell_4 H$, $\ell_i > 0$. Differentiating along the solutions and using the comparison principle bound $(S + (1 - \epsilon_v)V)/N \le (S^0 + (1 - \epsilon_v)V^0)/N^0$ proved in Appendix A3, we have

$$\begin{aligned}\dot{\mathcal{L}} \le\ & [\ell_1 f - \ell_1\phi + \ell_3\theta + \ell_4\zeta_c]I_c + [\ell_2\lambda_k S^0/N^0 - \ell_2\phi_k + \ell_4\zeta_k]I_k \\ & + [\ell_1 f + \ell_2\gamma_{ck} - \ell_3\phi_{ck} + \ell_4\zeta_{ck}]I_{ck} + [\ell_1 f + \ell_2(1 - p)\gamma_h - \ell_4\psi]H,\end{aligned}$$

where the the contribution of $\ell_2(1 - p)\gamma_h$ to the H-bracket arises from the back-flow into I_k.

Choosing $\ell_1 = 1$, $\ell_2 = 1$, $\ell_4 = (f + (1 - p)\gamma_h)/\psi$, $\ell_3 = \phi(1 - \mathcal{R}_{0c})/\theta \ge 0$ (when $\mathcal{R}_{0c} \le 1$) yields

$$\dot{\mathcal{L}} \le \phi(\mathcal{R}_{0c} - 1)I_c + \phi_k(C_k - 1)I_k + CI_{ck},$$

with $C < 0$ in the calibrated regime. Hence, $\dot{\mathcal{L}} \le 0$ when $\mathcal{R}_0 < 1$ and $C_k < 1$, with equality on $\{I_c = I_k = I_{ck} = H = 0\}$. On this invariant set, the remaining equations $\dot{S} = \Lambda + \pi R - (\eta + \mu)S$, $\dot{V} = \eta S - \mu V$, and $\dot{R} = -(\mu + \pi)R$ drive $R \to 0$ at a rate $\mu + \pi$, $S \to S^0$, and $V \to V^0$. The largest invariant set is $\{E_0\}$. By LaSalle [50], every trajectory in Ω converges to E_0. □

C4. Proof of Theorem 3.12

Proof. Relabel $x_1 = S$, $x_2 = V$, $x_3 = I_c$, $x_4 = I_k$, $x_5 = I_{ck}$, $x_6 = H$, and $x_7 = R$. The corrected system has $\dot{x}_7 = \gamma_c x_3 + p\gamma_h x_6 - (\mu + \pi)x_7$, and all β_c entries in the Jacobian carry the explicit $1/N^0$ scaling.

Take β_c as bifurcation parameter; let β_c^* satisfy $\mathcal{R}_{0c} = 1$. By Theorem 3.10, $J(E_0, \beta_c^*)$ has six eigenvalues with negative real parts (including $-(\mu + \pi)$ from the R-row) and a simple zero eigenvalue arising from the $x_3 = I_c$ row. Let w, v be the right and left eigenvectors with $vw = 1$ and $w_3, v_3 > 0$.

The non-zero second derivatives, with the $1/N^0$ scaling made explicit, are:

$$\frac{\partial^2 f_3}{\partial x_1 \partial x_3} = \frac{\beta_c^*}{N^0}, \qquad \frac{\partial^2 f_3}{\partial x_2 \partial x_3} = \frac{(1-\epsilon_v)\beta_c^*}{N^0}, \qquad \frac{\partial^2 f_3}{\partial x_3 \partial \beta_c} = \frac{x_1^0 + (1-\epsilon_v)x_2^0}{N^0}.$$

Substitution gives

$$\mathfrak{a} = -\frac{2v_3 w_1 w_3 \beta_c^* \phi(\eta + \mu)}{\Lambda} < 0, \qquad \mathfrak{b} = v_3 w_3 \frac{x_1^0 + (1-\epsilon_v)x_2^0}{N^0}\phi > 0,$$

with $\phi = \theta + \zeta_c + \gamma_c + \mu_c + \mu$. The splitting fraction p does not enter the bifurcation coefficients because the second-order spatial non linearities arise from the β_c coupling in the x_3 equation, not from the γ_h recovery in the x_6 equation.

Since $\mathfrak{a} < 0$ and $\mathfrak{b} > 0$, the bifurcation at $\mathcal{R}_{0c} = 1$ is forward (supercritical). The COVID-19 dominant boundary equilibrium E^* (with $I_k^* = I_{ck}^* = 0$) is locally asymptotically stable for $\mathcal{R}_{0c} > 1$, and no backward bifurcation occurs. □